A&A 651, A36 (2021)
https://doi.org/10.1051/0004-6361/202038259

Astronomy & Astrophysics

Probing the structure of a massive filament: ArTéMiS 350 and 450 μm mapping of the integral-shaped filament in Orion A⋆,⋆⋆

F. Schuller[1,2], Ph. André[1], Y. Shimajiri[3,1], A. Zavagno[4], N. Peretto[5], D. Arzoumanian[6,4], T. Csengeri[7], V. Könyves[8], P. Palmeirim[6], S. Pezzuto[9], A. Rigby[5], H. Roussel[10], H. Ajeddig[1], L. Dumaye[1], P. Gallais[1], J. Le Pennec[1], J. Martignac[1], M. Mattern[1], V. Revéret[1], L. Rodriguez[1], and M. Talvard[1]

[1] Laboratoire d'Astrophysique (AIM), CEA, CNRS, Université Paris-Saclay, Université Paris Diderot, Sorbonne Paris Cité, 91191 Gif-sur-Yvette, France
[2] Leibniz-Institut für Astrophysik Potsdam (AIP), An der Sternwarte 16, 14482 Potsdam, Germany
e-mail: fschuller@aip.de
[3] National Astronomical Observatory of Japan, Osawa 2-21-1, Mitaka, Tokyo 181-8588, Japan
[4] Université Aix Marseille, LAM & Institut Universitaire de France, 38 rue F. Joliot-Curie, 13388 Marseille CEDEX 13, France
[5] Cardiff University, School of Physics & Astronomy, Queen's buildings, The parade, Cardiff CF24 3AA, UK
[6] Instituto de Astrofísica e Ciências do Espaço, Universidade do Porto, CAUP, Rua das Estrelas, 4150-762 Porto, Portugal
[7] Laboratoire d'Astrophysique de Bordeaux, Univ. Bordeaux, CNRS, B18N, allée Geoffroy Saint-Hilaire, 33615 Pessac, France
[8] Jeremiah Horrocks Institute, University of Central Lancashire, Preston PR1 2HE, UK
[9] INAF-IAPS, Via Fosso del Cavaliere 100, Rome, Italy
[10] Institut d'Astrophysique de Paris, Sorbonne Université, CNRS (UMR 7095), 98 bis bd. Arago, 75014 Paris, France

Received 24 April 2020 / Accepted 7 April 2021

ABSTRACT

Context. The Orion molecular cloud is the closest region of high-mass star formation. It is an ideal target for investigating the detailed structure of massive star-forming filaments at high resolution and the relevance of the filament paradigm for the earliest stages of intermediate- to high-mass star formation.
Aims. Within the Orion A molecular cloud, the integral-shaped filament (ISF) is a prominent, degree-long structure of dense gas and dust with clear signs of recent and ongoing high-mass star formation. Our aim is to characterise the structure of this massive filament at moderately high angular resolution (8″ or ∼0.016 pc) in order to measure the intrinsic width of the main filament, down to scales well below 0.1 pc, which has been identified as the characteristic width of filaments.
Methods. We used the ArTéMiS bolometer camera at APEX to map a $\sim 0.6 \times 0.2$ deg^2 region covering OMC-1, OMC-2, and OMC-3 at 350 and 450 μm. We combined these data with *Herschel*-SPIRE maps to recover extended emission. The combined *Herschel*-ArTéMiS maps provide details on the distribution of dense cold material, with a high spatial dynamic range, from our 8″ resolution up to the transverse angular size of the map, ∼10–15′. By combining *Herschel* and ArTéMiS data at 160, 250, 350, and 450 μm, we constructed high-resolution temperature and H_2 column density maps. We extracted radial intensity profiles from the column density map in several representative portions of the ISF, which we fitted with Gaussian and Plummer models to derive their intrinsic widths. We also compared the distribution of material traced by ArTéMiS with that seen in the higher-density tracer N_2H^+(1–0) that was recently observed with the ALMA interferometer.
Results. All the radial profiles that we extracted show a clear deviation from a Gaussian, with evidence for an inner plateau that had not previously been seen clearly using *Herschel*-only data. We measure intrinsic half-power widths in the range 0.06–0.11 pc. This is significantly larger than the Gaussian widths measured for fibres seen in N_2H^+, which probably only traces the dense innermost regions of the large-scale filament. These half-power widths are within a factor of two of the value of ∼0.1 pc found for a large sample of nearby filaments in various low-mass star-forming regions, which tends to indicate that the physical conditions governing the fragmentation of pre-stellar cores within transcritical or supercritical filaments are the same over a large range of masses per unit length.

Key words. stars: formation – stars: massive – ISM: structure – submillimeter: ISM – ISM: individual objects: Orion A

1. Introduction

It is well established that star formation takes place in dense molecular clumps embedded in large molecular clouds. The evolution of these dense clumps towards the onset of gravitational collapse and the formation of solar-type stars is relatively well understood in outline, but several key questions remain unanswered, including how the star formation rate and efficiency depend on the environmental conditions and whether there are

⋆ The temperature and column density maps are only available at the CDS via anonymous ftp to cdsarc.u-strasbg.fr (130.79.128.5) or via http://cdsarc.u-strasbg.fr/viz-bin/cat/J/A+A/651/A36

⋆⋆ This publication is based on data acquired with the Atacama Pathfinder Experiment (APEX), project 098.F-9304. APEX is a collaboration between the Max-Planck-Institut für Radioastronomie, the European Southern Observatory, and the Onsala Space Observatory.

notable differences in the physical processes leading to the formation of low-mass and high-mass stars.

The *Herschel* Space Observatory has revealed ubiquitous filamentary structures in the cold interstellar medium (ISM; e.g. André et al. 2010; Molinari et al. 2010; Arzoumanian et al. 2011, 2019; Schisano et al. 2020). Many subsequent studies, including theoretical work (e.g. Federrath 2016), have confirmed how important filaments are to the evolution of interstellar matter and star formation activity, and they have supported a filament paradigm for star formation (see the review by André et al. 2014). However, most detailed (resolved) studies to date have concentrated on a few, typically nearby clouds, where mostly low-mass and solar-type stars are forming (Arzoumanian et al. 2011; Hacar et al. 2013; Könyves et al. 2015, among others).

The Orion A giant molecular cloud is the nearest site of active star formation that includes high-mass stars. At a distance of only 410 pc (Menten et al. 2007; Stutz et al. 2018), it is an ideal target for investigating the initial phases of high-mass star formation in great detail. It is located within the Barnard's Loop, which is part of a large complex of bubbles and filaments in a superbubble (Ochsendorf et al. 2015). A large filamentary structure with a length of several tens of parsecs is seen along the north-south direction across Orion A. The densest part of this filament is a ∼1.5 deg long structure (∼10 pc if in the plane of the sky) known as the integral-shaped filament (ISF; Bally et al. 1987). This structure is clearly visible in dust continuum emission (Nutter & Ward-Thompson 2007; Shimajiri et al. 2011) or in CO molecular lines (Kong et al. 2018; Suri et al. 2019). The Orion Nebula Cluster (ONC) appears approximately projected on the middle of this dense filament.

On large physical scales (0.05–8.5 pc), Stutz & Gould (2016) concluded from the analysis of *Herschel* data at ∼36″ angular resolution that the radial distribution of the gas surface density near the ISF follows a power law. At much higher angular resolution (4.5″), using data in the high-density tracer N_2H^+(1–0) line obtained with the Atacama Large Millimeter/Sub-millimter Array (ALMA), Hacar et al. (2018) argued that the ISF contains a large number of fibres organised in a complex network. They measured emission profiles characterised by full widths at half maximum (FWHMs) in the range 0.015–0.065 pc, with a median value of 0.035 pc, which is significantly smaller than the typical 0.1 pc half-power width derived from *Herschel* column density maps in a number of nearby molecular complexes (Arzoumanian et al. 2011, 2019). Since these column density maps were derived from dust thermal emission in the sub-millimetre, they also trace lower-density material than the N_2H^+(1–0) transition. Therefore, the question remains open as to whether the observed difference in filament widths can be explained by the difference in the angular resolution of the data, or if they trace different material with different physical conditions.

With an angular resolution of 8″ at 350 µm, more than three times better than *Herschel* at the same wavelength, the ArTéMiS camera installed at the Atacama Pathfinder Experiment (APEX) 12 m telescope (Revéret et al. 2014; André et al. 2016) is an ideal tool for probing the cold, dusty ISM at <0.1 pc scale up to distances of ∼3 kpc. We observed a ∼0.1 deg^2 region covering the northern end of the ISF with this instrument at 350 and 450 µm. The ArTéMiS maps, combined with *Herschel* data, provide a detailed view, with a large spatial-dynamic range, of the distribution of cold gas and dust, allowing us to draw an accurate picture of the ISF and its substructures. We describe the data that we use in Sect. 2. We then present our measurements of the radial intensity profiles along several portions of the main filament in Sect. 3. We discuss our results and compare them with previous findings in Sect. 4. Finally, we summarise our conclusions in Sect. 5.

2. Observations and data reduction

2.1. Herschel data

As part of the *Herschel* Gould Belt Survey (HGBS) key project (André et al. 2010), a large map of 22 deg^2 covering the Orion A cloud and nebula was observed at 70, 160, 250, 350, and 500 µm. Details regarding the HGBS standard data reduction and calibration procedure can be found in Könyves et al. (2015, 2020). In particular, the emission seen on the largest scales should be accurate since zero-level offsets as estimated from *Planck* and IRAS data were applied (cf. Bernard et al. 2010).

Initial results from the HGBS observations towards Orion A were published by: Roy et al. (2013), who investigated the physical properties of the dust in this region; Stutz et al. (2013), who made a systematic census of the reddest protostars; and Polychroni et al. (2013), who found two different core mass functions for cores within and out of the filaments. Here, we focus on the northern part of the Orion A cloud, which covers a large fraction of the ISF, including OMC 1, OMC 2, and OMC 3.

The *Herschel*-SPIRE parallel-mode data are affected by saturation in the vicinity of the bright source Orion-KL: 55 pixels cannot be used in the original (10″ pixel^{-1}) map at 350 µm, nor can 14 pixels be used in the original (14″ pixel^{-1}) map at 500 µm. We corrected for this by using dedicated SPIRE-only data taken towards Orion-KL and interpolating the values measured on neighbouring pixels. This leads to an extra uncertainty in the flux calibration for this region, which covers ∼0.7′× 2′, a scale well probed by the ArTéMiS observations (see below).

2.2. ArTéMiS observations

New observations were conducted with ArTéMiS, which is installed at the APEX telescope (Güsten et al. 2006) in Chile. The first maps were acquired in July 2013, during the commissioning run of the first incarnation of the camera, with only one focal plane at 350 µm. Most observations were done with the current version of ArTéMiS (Talvard et al. 2018), which covers the same ∼5 × 2.5 arcmin^2 field of view at 350 and 450 µm, in several runs between October and December 2016. All observations consist of large on-the-fly maps, with scanning speeds of 20″ s^{-1} and 60″ s^{-1} and steps between lines of 5″ and 30″ for the data taken in 2016 and in 2013, respectively. In total, about 16 hr were spent on-source.

The weather conditions were generally very good, with a total amount of precipitable water vapour (PWV) between 0.25 and 0.7 mm. The zenith opacity at 350 and 450 µm was frequently measured with skydip observations and found to be between 0.8 and 1.2 at 350 µm and between 0.6 and 1.1 at 450 µm. The absolute flux calibration was checked and corrected for using maps of the primary calibrator Uranus and several secondary calibrators (NGC 253, NGC 2071, and CRL 618). The overall calibration uncertainty is estimated to be ∼30% at 350 µm and ∼20% at 450 µm.

2.3. ArTéMiS data reduction

The ArTéMiS data at 350 and 450 µm were processed with the dedicated IDL pipeline, which takes care of converting the raw data to IDL-friendly data structures, applying flux calibration, and rejecting unusable pixels. Special care was taken to correct

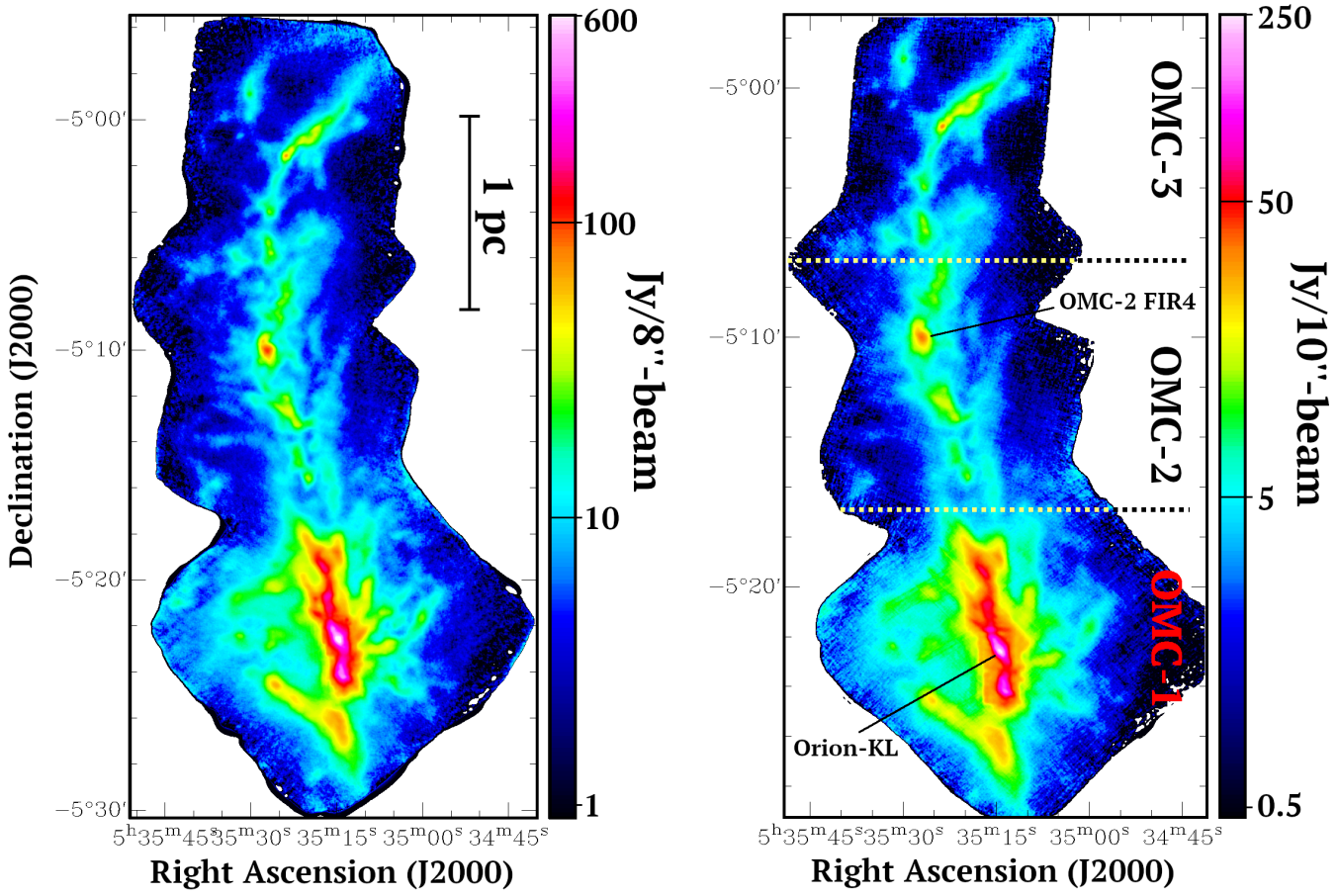

Fig. 1. ArTéMiS maps at 350 µm combined with *Herschel*-SPIRE data at 350 µm (*left*) and ArTéMiS maps at 450 µm combined with *Herschel*-SPIRE data at 500 µm (*right*), shown in logarithmic colour scale. Some regions discussed in the text are indicated in the *right panel*.

for possible pointing errors between individual maps before a combined map could be computed. Then, the data were processed with a tailored version of the *Scanamorphos* software adapted for ArTéMiS data (Roussel 2013, 2018). This pipeline makes use of the redundancy in the data to properly separate the various sources of noise (especially sky noise) from the real signal. This allows us to recover emission at scales that are usually filtered out by the typical data reduction of ground-based bolometer observations because such emission mimics the sky emission.

In order to recover extended emission at even larger scales, we combined the ArTéMiS maps with *Herschel*-SPIRE maps at similar wavelengths using the *immerge* task in MIRIAD (Sault et al. 1995). The *immerge* algorithm combines the available data in the Fourier domain after determining an optimal calibration factor to align the flux scales of the input images (here from ArTéMiS and SPIRE) in a common annulus of the uv plane. Here, we adopted an annulus corresponding to the range of baselines from 0.5 m (baseline b, sensitive to angular scales $\lambda/\mathrm{b} \sim 2.4'$ at $\lambda = 350$ µm) to 3.5 m (the diameter of the *Herschel* telescope) to align the flux scale of the ArTéMiS 350 µm map to the flux scale of the SPIRE 350 µm map. We used the same method to combine the ArTéMiS 450 µm data with *Herschel*-SPIRE maps at 500 µm, which is the nearest wavelength observed with SPIRE.

The combined maps at 350 and 450 µm, covering about 30×10 arcmin^2, are shown in Fig. 1. The effective resolution is ∼8″ and ∼10″ (FWHM) at 350 and 450 µm, respectively. The typical rms noise in this mosaic is between 0.3 and 0.5 Jy/8″-beam in regions with no strong emission at 350 µm. The discussion in the rest of the article is based on this combined *Scanamorphos*-processed ArTéMiS and SPIRE map. We stress that the ArTéMiS observations allow us not only to improve the angular resolution compared to *Herschel*, but also to properly measure the peak of the emission towards Orion-KL, where the SPIRE emission maps are saturated.

2.4. Archival ALMA observations in N_2H^+

Hacar et al. (2018) combined newly obtained ALMA data with data from the IRAM 30 m telescope to build a map in $N_2H^+(1–0)$ at 4.5″ resolution. They report the detection of 55 fibre-like structures, with typical FWHMs (as derived from Gaussian fitting) in the range 0.02–0.06 pc. We discuss the associations of these fibre-like structures with the large-scale filament seen in sub-millimetre continuum in Sect. 4.2.

3. Radial profile analysis

3.1. High-resolution temperature and column density maps

In order to characterise the physical structures present in our maps, we first derived a map of H_2 column density at the highest possible angular resolution, using the following method. First, we re-projected the *Herschel*-PACS, SPIRE 250 µm, ArTéMiS–SPIRE 350 µm, and ArTéMiS 450 µm–SPIRE 500 µm maps

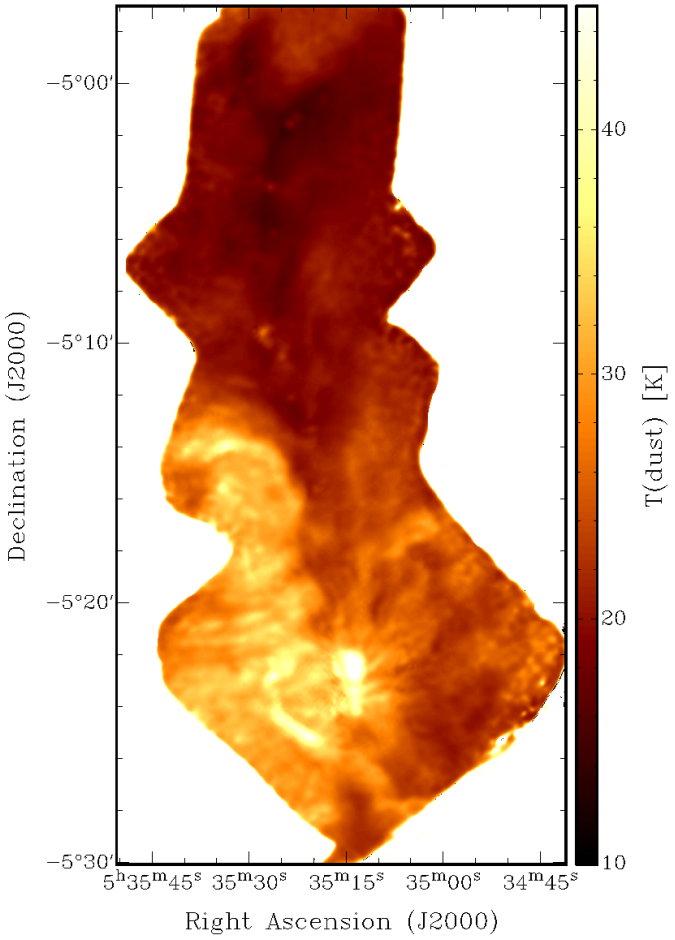

Fig. 2. Dust temperature map at 18″ resolution, derived from the combined analysis of ArTéMiS and *Herschel*–PACS+SPIRE data.

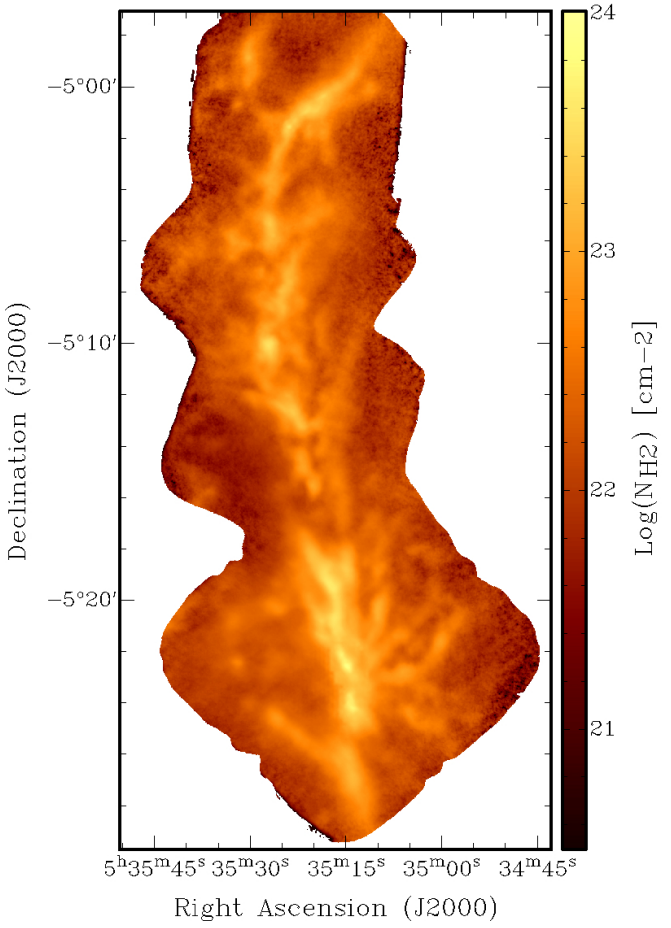

Fig. 3. Column density map at ∼8″ resolution, derived from the 350 μm emission map and the temperature map shown in Fig. 2, assuming the uniform dust opacity law given by Eq. (1) (see text for details).

to a common grid and smoothed all data to a common angular resolution of 18.2″ (the lowest resolution of the above four maps, set by the SPIRE 250 μm data). We then generated a dust temperature map at 18.2″ resolution by fitting a modified blackbody of the form $B_\nu(T_\mathrm{d}) \times \kappa_\nu$ to the four measurements between 160 μm and 500 μm on a pixel-by-pixel basis, where $B_\nu(T_\mathrm{d})$ is the *Planck* blackbody function at frequency ν (or wavelength λ) for a dust temperature T_d and κ_ν (or κ_λ) is the dust opacity. For simplicity and easier comparison with *Herschel* work, our nominal assumption for the dust opacity law is the same as that adopted in HGBS papers:

$$\kappa_\lambda = 0.1 \times (\lambda/300\ \mu\mathrm{m})^{-\beta}\ \mathrm{cm}^2\ \mathrm{per\ g\ of\ gas + dust} \quad (1)$$

with an emissivity index $\beta = 2$ (Hildebrand 1983; Roy et al. 2014). The resulting dust temperature map is shown in Fig. 2. The dust temperature values range from 14 to 25 K in the northern part of our map, and from 22 to 52 K in the southern part, with the largest values (above 45 K) only found towards the Orion-KL HII region. The general trends seen in our map agree well with the temperature map published by Lombardi et al. (2014) based on *Herschel* data only, but our data provide a better spatial resolution and allow us to properly estimate the temperature around the Orion-KL region, where the *Herschel* data are affected by saturation.

In a second step, we converted the ArTéMiS-SPIRE 350 μm intensity map to a high-resolution (∼8″) column density map, assuming a fixed dust temperature at each position given by the temperature map obtained in the first step at somewhat lower resolution. Assuming optically thin dust emission, the specific intensity I_{350} (in MJy sr^{-1}) at $\lambda = 350$ μm was converted to H_2 column density as follows:

$$N_{\mathrm{H}_2} = I_{350}/(B_{350}[T_\mathrm{d}]\kappa_{350}\mu_{\mathrm{H}_2} m_\mathrm{H}), \quad (2)$$

where $\mu_{\mathrm{H}_2} = 2.8$ is the mean molecular weight. The resulting column density map is shown in Fig. 3 and is publicly available from the CDS.

Uncertainties in the dust opacity law induce uncertainties in the derived temperature and column density maps. The temperature map does not depend on the normalisation of the dust opacity law but is somewhat sensitive to the assumed value of the emissivity index (β), although the effect is rather small. For instance, changing β from 2 to 1.5 would only increase the dust temperatures by ∼20% in the northern part and by ∼35% on average in the southern part of the main filament. This would in turn decrease the derived column densities by ∼50% and ∼70% on average in the northern and southern parts, respectively. Observationally, the spectral index map obtained between 450 μm and 850 μm by Johnstone & Bally (1999) with SCUBA is consistent with $1.5 \lesssim \beta \lesssim 2$ in the bulk of the ISF region. In their multi-wavelength study of the OMC–2/3 subregion, Sadavoy et al. (2016) find $\beta = 1.7$–1.8. Lower, more extreme values of β may apply locally to compact dense cores or very bright objects, such

as OMC–3 MM6 or Orion KL, but these values have only a limited impact on the present study, which is focused on the main filament.

On the other hand, the column density map scales directly with the adopted normalisation of the dust opacity law at 300 µm, κ_{300}. Based on a comparison of the *Herschel* results with a near-infrared extinction map of Orion A from 2MASS, Roy et al. (2013) find evidence of a weak trend between dust opacity and column density, $\kappa_{300} \propto N_{\rm H_2}^{0.28}$, in the regime $1 \lesssim A_{\rm V} \lesssim 10$ mag, which they interpreted as a signature of dust grain evolution. Assuming this correlation between κ_{300} and $N_{\rm H_2}$ continues at higher $A_{\rm V}$, the default value assumed here for κ_{300} should remain valid within 60% accuracy for $3\times10^{21}\,{\rm cm^{-2}} \lesssim N_{\rm H_2} \lesssim 10^{23}\,{\rm cm^{-2}}$ (see Roy et al. 2014). Along the spine of the integral filament where $N_{\rm H_2}$ exceeds $10^{23}\,{\rm cm^{-2}}$, the actual value of κ_{300} may be a factor of 2–2.5 higher than our default value. In turn, the map shown in Fig. 3 may overestimate the actual column density along the spine of the integral filament by a factor of ~2–2.5. Significant changes in dust opacity may also occur in the Orion bar and the photodissociation region around the HII region (cf. Salgado et al. 2016), but these changes do not affect our analysis of the structure of the ISF away from OMC–1.

To summarise and illustrate the influence of dust opacity uncertainties, we derived alternative temperature and column density maps from a two-parameter fitting similar to that employed for Figs. 2 and 3 but using the following alternative opacity law instead of the nominal HGBS opacity law:

$$\kappa_\lambda = 0.1\times(N_{\rm H_2}/N^0_{\rm H_2})^{0.28}\times(\lambda/300\ {\rm \mu m})^{-\beta(N_{\rm H_2})}\ {\rm cm^2 g^{-1}}, \quad (3)$$

where $N^0_{\rm H_2} = 1.7\times10^{22}\,{\rm cm^{-2}}$ and $\beta(N_{\rm H_2}) = \{2\times[100 - (N_{\rm H_2}/10^{21})] + 1.5\times[(N_{\rm H_2}/10^{21}) - 1]\}/99$ (i.e. a dust emissivity index decreasing linearly between $\beta = 2$ at $N_{\rm H_2} = 10^{21}\,{\rm cm^{-2}}$ and $\beta = 1.5$ at $N_{\rm H_2} = 10^{23}\,{\rm cm^{-2}}$). This alternative opacity law combines the trend found by Roy et al. (2013) with a plausible variation in β with column density. We show the results in Appendix A, in the form of maps of relative difference in temperature, $(T_{\rm d}^{\rm alt} - T_{\rm d}^{\rm std})/T_{\rm d}^{\rm std}$ (Fig. A.1), and column density, $(N_{\rm H_2}^{\rm alt} - N_{\rm H_2}^{\rm std})/N_{\rm H_2}^{\rm std}$ (Fig. A.2), between the alternative maps ($T_{\rm d}^{\rm alt}$, $N_{\rm H_2}^{\rm alt}$) derived using Eq. (3) and the nominal maps ($T_{\rm d}^{\rm std}$, $N_{\rm H_2}^{\rm std}$) derived using Eq. (1). As expected, the alternative dust temperature map has slightly higher values than the nominal dust temperature map (Fig. 2), by ~10–20% in the bulk of the integral filament and up to ~50% towards Orion KL (see Fig. A.1). In the OMC-1 subregion, and especially in the immediate vicinity of Orion KL, the spectral energy distributions (SEDs) peak at wavelengths shorter than 160 µm and the dust temperature derived from measurements made longward of 160 µm is more uncertain. Accordingly, the alternative column density map has lower values than the nominal column density map (Fig. 3) by up to a factor of ~3–4 towards Orion KL and only a factor of ~2 along the bulk of the integral filament (see Fig. A.2).

3.2. Extraction of filamentary structures

We applied the DisPerSE algorithm (Sousbie 2011) to a version of the ArTéMiS+SPIRE 350 µm image smoothed to 16″ resolution to trace the crests of the most prominent filamentary structures seen in our data, including the spine of the ISF. Apart from the main filament (i.e. the ISF), DisPerSE identified a network of fainter filamentary structures, most of which correspond to sub-filaments or branches directly connected to the ISF, especially in the OMC-1 region (see Fig. 4).

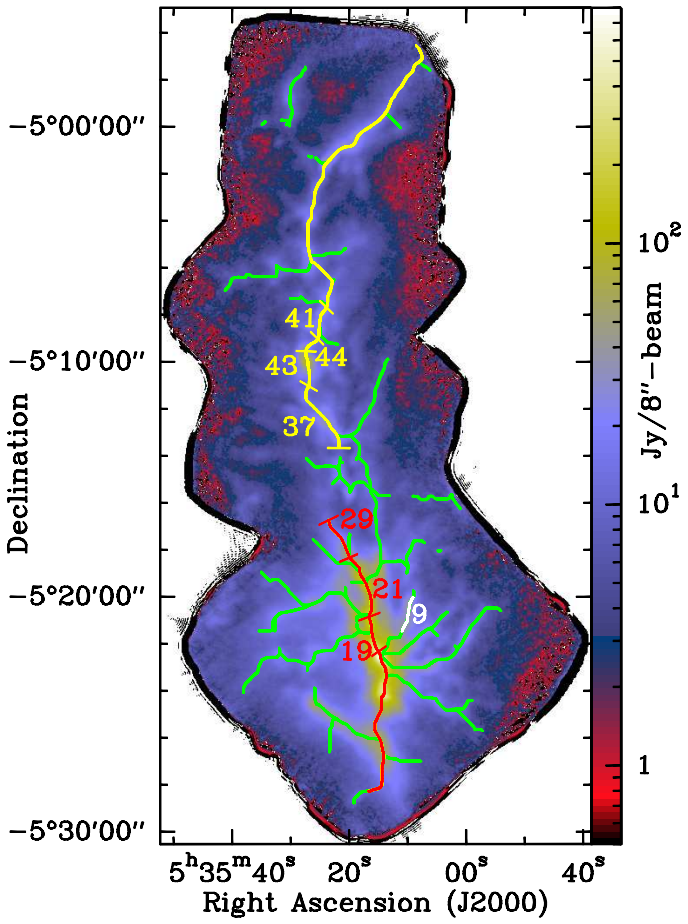

Fig. 4. Skeleton map with the filament crests identified with DisPerSE overlaid on the ArTéMiS +SPIRE 350 µm map (logarithmic colour scale). The numbers mark filament segments roughly corresponding to the N_2H^+ fibres discussed by Hacar et al. (2018), as listed in Col. 1 of Table 1. The yellow crest corresponds to the ISF portion referred to as 'ISF-OMC-2/3' in the text, and the red one corresponds to 'ISF-OMC-1'.

In the present paper, we mostly focus our analysis on the density structure of the main filament, whose DisPerSE crest is highlighted in red and yellow in Fig. 4. We stress that the definition of this main crest depends only weakly on the algorithm used to trace filamentary structures. In particular, we verified that the crests obtained with the alternative algorithms *FilFinder* (Koch & Rosolowsky 2015) and *getsf* (Men'shchikov 2021) are very similar to that shown in Fig. 4 from DisPerSE (cf. Fig. B.1). Indeed, filament-finding algorithms tend to yield consistent results for high-contrast filaments such as the ISF.

We constructed radial density profiles by taking perpendicular cuts at each pixel of the 8″ resolution column density map along each filament crest, using a similar method to that used by André et al. (2016) for NGC 6334. The column density profiles derived for the northern (OMC-2 and OMC-3) and southern (OMC-1) parts of the main filament (the ISF) are shown in Figs. 5–7. We also investigated a smaller, relatively isolated filament (marked with the number 9 in Fig. 4) in the south-western part of our map.

3.3. Fits to the radial profiles

To estimate the physical width of each filament, we fitted the median column density profiles with both Gaussian and

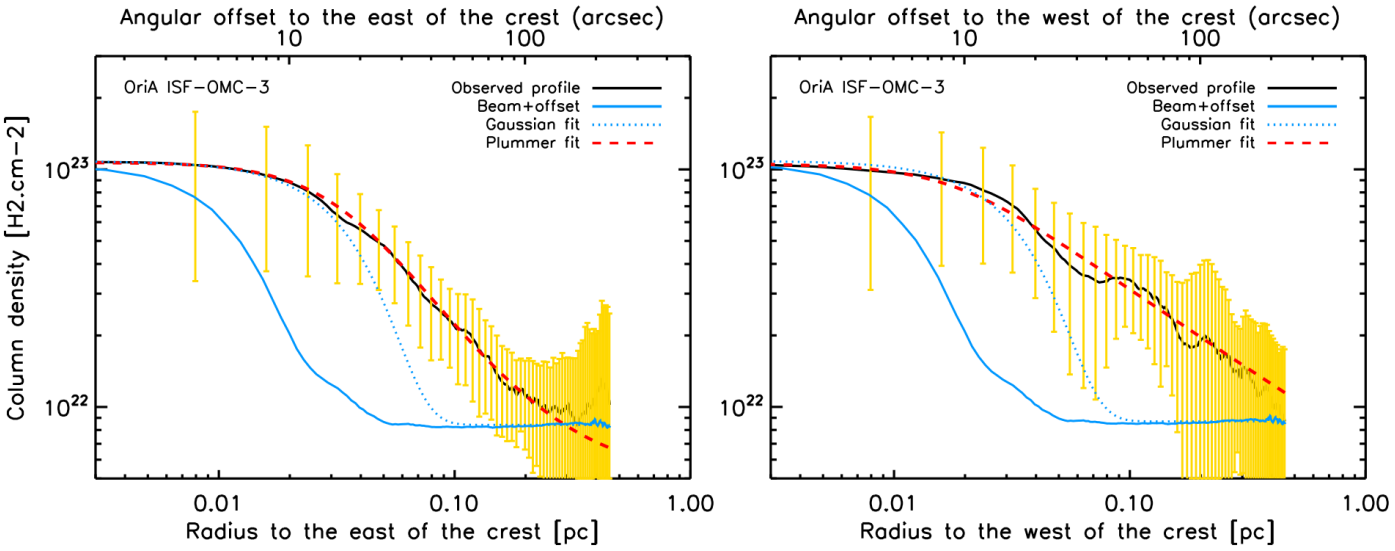

Fig. 5. Median radial profiles for the northernmost part of the ISF (solid black curves), covering OMC-3, measured on the H_2 column density map perpendicular to the filament crest (see Fig. 4), on the eastern (*left panel*) and western (*right panel*) sides of the filament. One data point is shown every half beam (Nyquist sampling). The yellow error bars show the ($\pm 1\sigma$) dispersion of the distribution of radial profiles observed along the filament crest. The solid blue curves show the effective beam profile of the ArTéMiS 350 µm data shifted by a constant offset corresponding to the typical background observed nearby. The dotted blue curves show the best-fit Gaussian (plus constant offset) model to the inner part of the observed profile, and the dashed red curves show the best-fit Plummer model (convolved with the beam) on either side of the filament crest.

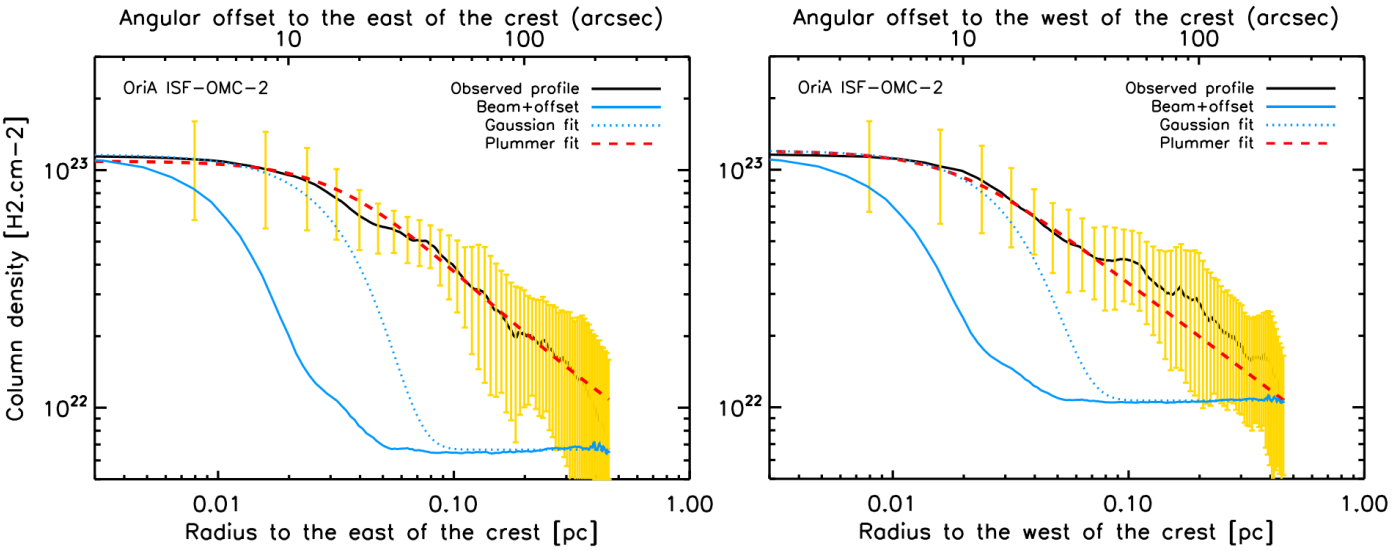

Fig. 6. Same as Fig. 5 but for the portion of the main filament covering the OMC-2 region.

Plummer-like functions. We fitted the two sides of each filament separately to account for strongly varying background emission. We also cut the main filament into three portions, corresponding to the OMC-1, OMC-2, and OMC-3 subregions as marked in Fig. 1, to account for the varying physical conditions between the northern and southern part of our map. While it is clear that other nearby features can affect individual measurements, the use of median profiles allows us to derive the average global properties of each portion of the main filament.

Most of the filamentary structures observed here exhibit power-law emission wings, such that Gaussian functions do not reproduce their entire radial profiles well, as is evident in Figs. 5–7. Only the inner part of the radial profiles was thus fitted with a Gaussian function. To do so, the width of each column density profile at half power above the background emission was first roughly estimated using the closest point to the filament crest for which the logarithmic derivative of the profile, $\mathrm{d}\ln N_{\mathrm{H_2}}/\mathrm{d}\ln r$, showed a significant switch from negative to positive (or negligible) values. The observed profile was then fitted with a Gaussian function over a range of radii corresponding to twice this initial width estimate.

The Plummer-like model function that was fitted to the full radial profile of H_2 column density ($N(r)$, after convolution with the approximately Gaussian ~8″ beam of the observations) is the following:

$$N_{\mathrm{Plummer}}(r) = N_0/[1 + (r/R_{\mathrm{flat}})^2]^{\frac{p-1}{2}} + N_{\mathrm{bg}}, \quad (4)$$

where R_{flat} is the radius of the flat inner region with roughly constant emission in the profile, p is the power-law exponent of the

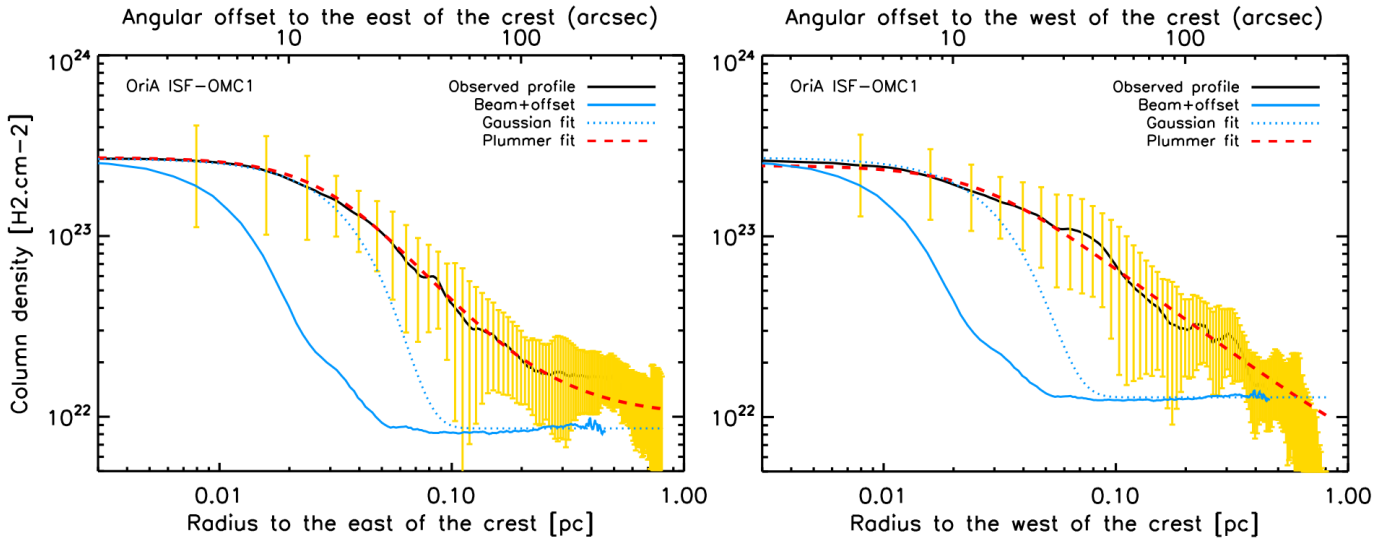

Fig. 7. Same as Fig. 5 but for the southern part of the main filament (including the OMC-1 region).

profile at radii larger than $R_{\rm flat}$, N_0 is the central column density, and $N_{\rm bg}$ is the column density of the background cloud. A more detailed description of the fitting procedure is given in Sect. 3 of Arzoumanian et al. (2019). For a cylindrical model filament with a Plummer-like column density profile following Eq. (4), the underlying volume density profile has a similar form:

$$n_{\rm Plummer}(r) = \frac{n_0}{\left[1 + (r/R_{\rm flat})^2\right]^{p/2}}, \quad (5)$$

where n_0 is the central volume density of the filament. Moreover, n_0 is related to the projected central column density (N_0) by the simple relation $n_0 = N_0/(A_p\, R_{\rm flat})$, where $A_p = \frac{1}{\cos i} \times B\left(\frac{1}{2}, \frac{p-1}{2}\right)$ is a constant factor that depends on the inclination angle (i) of the filament to the plane of sky and B is the Euler beta function (cf. Palmeirim et al. 2013).

3.4. Results

We report the best-fit values of $D_{\rm flat} \equiv 2 \times R_{\rm flat}$ and p from Plummer fitting, as well as the deconvolved FWHMs from Gaussian fitting, for several segments of the ISF in Table 1. As pointed out by several authors, the errors in $D_{\rm flat}$ and p are significantly correlated, leading to some degeneracy in the derivation of these two parameters (e.g. Malinen et al. 2012; Smith et al. 2014; Arzoumanian et al. 2019). For this reason, we also provide, in the fifth column of Table 1, the half-power diameter derived from Plummer fitting:

$$D_{\rm HP}^{\rm Plummer} = \sqrt{2^{\frac{2}{p-1}} - 1} \times D_{\rm flat}, \quad (6)$$

defined by

$$N_{\rm Plummer}(D_{\rm HP}^{\rm Plummer}/2) = N_0/2 + N_{\rm bg}. \quad (7)$$

The advantage of $D_{\rm HP}^{\rm Plummer}$ is that it is a more robust estimator of the inner width of a Plummer-like profile than $D_{\rm flat}$ because its derivation is not as strongly correlated to that of p. It is worth pointing out that for high-contrast filaments ($N_{\rm bg} \ll N_0$) such as the ISF, $D_{\rm HP}$ depends only weakly on the background column density ($N_{\rm bg}$). We further show in Appendix B that $D_{\rm HP}$ is a robust quantity, affected by only small systematic errors ($\lesssim 30\%$) due to uncertainties in the dust opacity and the presence of temperature gradients along the line of sight.

The inner widths reported in Table 1 represent median values for each ISF segment, derived from a detailed fitting analysis of median column density profiles such as those shown in Figs. 5–7. As is evident from the yellow error bars in these figures, there are significant fluctuations in the profiles along the length of the ISF. To quantify the impact of these fluctuations on our filament width estimates, we display a histogram of 221 individual width measurements made at beam-spaced positions along the whole crest of the ISF in Fig. 8. The individual inner widths used in Fig. 8 do not result from any Gaussian or Plummer fitting but correspond to simpler half-maximum diameters estimated as twice the radius from the filament crest at which the background-subtracted amplitude of the observed radial profile is half of the value on the crest (see '*hd* widths' in Arzoumanian et al. 2019). Such simple *hd* width estimates are directly comparable to Gaussian FWHM or Plummer $D_{\rm HP}$ estimates, but they are more robust and less affected by outliers. (When checked and reliable, Gaussian and Plummer fits are nevertheless preferable since they provide a better characterisation of the filament profiles and additional information such as line mass and density estimates.) Figure 8 also compares the distribution of individual widths obtained here for the ISF (black histogram) with the distribution of widths found by Arzoumanian et al. 2019 (blue histogram). Although the latter is somewhat broader than the former, which is not surprising since it is based on a much broader sample of 599 filaments in eight nearby clouds at different distances, it can be seen that the two distributions have very similar overall shapes and peak at the same value, just below 0.1 pc.

Overall, we measure inner $D_{\rm HP}^{\rm Plummer}$ widths in the range of 0.06 to 0.11 pc, consistent within better than a factor of two with the half-power widths reported by Arzoumanian et al. (2019) for other Gould Belt filaments and by André et al. (2016) for the NGC 6334 filament ($D_{\rm HP}^{\rm Plummer} = 0.16 \pm 0.05$ pc at 1.7 kpc, or 0.12 ± 0.03 pc adopting a revised distance of 1.3 kpc to NGC 6334; cf. Chibueze et al. 2014). Particularly remarkable is the similarity in width with the Taurus B211/B213 filament ($D_{\rm HP}^{\rm Plummer} = 0.11 \pm 0.02$ pc – Palmeirim et al. 2013), which has an order of magnitude lower column density than the ISF. The errors given in Table 1 are only statistical fitting uncertainties.

Table 1. Median inner widths of selected filaments, as derived from both Plummer and Gaussian fitting to the observed radial column density profiles, and power-law indices of the best-fit Plummer profiles.

Fibre/	N_{H2} map (ArTéMiS + *Herschel*)				*FWHM* (Hacar et al. 2018)		
Filament	D_{flat} (pc)	p	*FWHM* (pc)	$D_{HP}^{Plummer}$ (pc)	min (pc)	max (pc)	median (pc)
ISF-OMC-3							
West	0.04 ± 0.01	1.7 ± 0.3	0.06 ± 0.02	0.08 ± 0.02			
East	0.05 ± 0.01	2.3 ± 0.3	0.06 ± 0.01	0.08 ± 0.01			
ISF-OMC-2							
West	0.045 ± 0.01	1.7 ± 0.3	0.06 ± 0.02	0.08 ± 0.02			
East	0.06 ± 0.01	2.0 ± 0.2	0.06 ± 0.01	0.11 ± 0.02			
Fibre 41 (W)	0.045 ± 0.01	2.0 ± 0.2	0.05 ± 0.01	0.08 ± 0.01	0.025	0.095	0.04
Fibre 41 (E)	0.06 ± 0.01	2.2 ± 0.3	0.05 ± 0.02	0.09 ± 0.02			
Fibre 44 (E)	(0.06 ± 0.02)	(2.0 ± 0.3)	0.06 ± 0.03	0.10 ± 0.03	0.045	0.065	0.06
Fibre 43 (W)	(0.04 ± 0.02)	(2.0 ± 0.3)	0.05 ± 0.01	(0.07 ± 0.02)	0.02	0.06	0.035
Fibre 43 (E)	(0.05 ± 0.02)	(2.3 ± 0.3)	(0.08 ± 0.02)	(0.07 ± 0.02)			
Fibre 37 (W)	(0.07 ± 0.03)	(2.0 ± 0.5)	(0.07 ± 0.02)	(0.09 ± 0.04)	0.03	0.11	0.05
Fibre 37 (E)	0.09 ± 0.03	2.4 ± 0.3	0.14 ± 0.03	0.11 ± 0.03			
ISF-OMC-1							
West	0.05 ± 0.01	2.0 ± 0.1	0.055 ± 0.01	0.085 ± 0.01			
East	0.05 ± 0.02	2.4 ± 0.3	0.06 ± 0.01	0.06 ± 0.02			
Fibre 29 (W)	(0.05 ± 0.02)	(2.3 ± 0.5)	0.05 ± 0.01	(0.07 ± 0.02)	0.025	0.040	0.035
Fibre 29 (E)	(0.06 ± 0.02)	(2.5 ± 0.5)	0.07 ± 0.01	0.11 ± 0.02			
Fibre 21 (W)	0.04 ± 0.01	(2.0 ± 0.3)	0.05 ± 0.01	0.07 ± 0.01	0.015	0.090	0.030
Fibre 21 (E)	(0.04 ± 0.02)	(2.0 ± 0.5)	0.05 ± 0.02	0.06 ± 0.01			
Fibre 19 (W)	(0.06 ± 0.01)	(2.0 ± 0.3)	0.07 ± 0.02	0.10 ± 0.02	0.005	0.030	0.020
Fibre 19 (E)	(0.04 ± 0.01)	(2.2 ± 0.3)	0.06 ± 0.01	0.06 ± 0.01			
Fibre 9 (W)	(0.04 ± 0.02)	(2.3 ± 0.5)	0.06 ± 0.01	0.06 ± 0.02	0.025	0.055	0.035

Notes. The fibre numbers (Col. 1) refer to the fibres discussed by Hacar et al. (2018) that we tentatively associate with some segments of the filaments seen with ArTéMiS (Sect. 4.2). Columns 2–5 give the parameters of the best-fit models on the H_2 column density map (Fig. 3); the values in Cols. 6–8 were extracted from Fig. 10 in Hacar et al. (2018) and refer to the structures seen in N_2H^+. Unless otherwise specified, the Plummer fits on either side of each filament segment were performed over the whole range of radii shown in Figs. 5–7, i.e. from 0 to ~0.45 pc, and the Gaussian fits from 0 to twice the simple half-power radius derived without any fitting (see text), i.e. typically ~0.08–0.1 pc. The western side of the OMC-2 segment was fitted with a Plummer model only out to a radius of 0.08 pc due to the presence of a shoulder in the background beyond that radius (see Fig. 6b); the eastern side of the OMC-1 segment was fitted out to a radius of 0.3 pc, and the western side of fibre 9 out to a radius of 0.1 pc. The values shown in parentheses denote cases where the column density profile does not exhibit clear evidence of a power-law wing (for example fibre 9; see Fig. 10), or where nearby emission strongly affects the measured profile, resulting in higher uncertainties in the fitted values.

To assess the importance of systematic errors due to uncertainties in the dust properties, we also performed a similar radial profile analysis on the alternative column density map derived using Eq. (3) instead of Eq. (1) for the dust opacity law. The results are provided in Table A.1. Generally speaking, the measured radial profiles tend to be slightly shallower, with slightly lower p index values (by $\delta p \sim 0.2$), in the alternative column density map. The inner widths derived from the alternative column density map range from 0.07 to 0.16 pc and are typically ~30% higher than those found with the default column density map. They remain consistent with the filament widths found by Arzoumanian et al. (2019). Overall, uncertainties in the dust opacity law have a stronger influence on the absolute level of the column density profiles than on the profile shapes and the derived filament widths.

We also verified that our results on the widths do not depend on the choice of the algorithm employed to trace the crest of the ISF (see Appendix B). In particular, a Kolmogorov-Smirnov test reveals that the three distributions of individual widths measured along the ISF using the DisPerSE, *FilFinder*, and *getsf* crests, respectively, are statistically indistinguishable (see Fig. B.2).

The inner widths that we measure are almost always larger than the 0.02–0.06 pc range of values derived by Hacar et al. (2018) from combined ALMA+IRAM 30 m observations in the high-density tracer N_2H^+(1–0). Because the N_2H^+(1–0) line is effectively tracing only dense gas with $n_{H_2} \gtrsim 10^4$ cm^{-3} (cf. Shirley 2015), it may not properly sample the outer parts of the underlying radial density profiles, therefore biasing the results towards lower width values.

The p exponents of the best-fit Plummer profiles for the various portions of the ISF are consistent with the typical values of $p = 2.2 \pm 0.3$ found by Arzoumanian et al. (2019) for a large sample of nearby *Herschel* filaments in the Gould Belt. For the northern part of the ISF, they are also roughly consistent with the power-law exponent $p = 1.5 \pm 0.5$ reported by Mattern et al. (2018) for another wide sample of almost 200

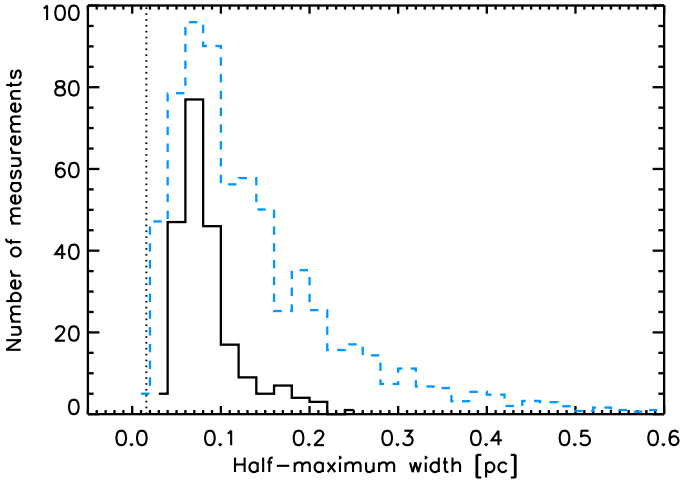

Fig. 8. Histogram of 221 independent individual width measurements made at beam-spaced positions along the whole (OMC-1 + OMC-2 + OMC-3) ISF (solid black line), compared to a similar histogram obtained by Arzoumanian et al. (2019) for a large sample of 599 filaments in eight nearby clouds (dashed blue line). The y-axis of the latter (blue) histogram was scaled down by a factor of 13 for easier comparison with the ISF histogram. The vertical dashed line marks the spatial resolution (∼0.016 pc) of the ArTéMiS 350 µm and column density maps used in this paper (Figs. 1 and 3). The median value of the OMC distribution (black histogram) is 0.075 pc, and the interquartile range is 0.03 pc. The median value of the blue distribution is 0.1 pc, and its interquartile range is 0.1 pc.

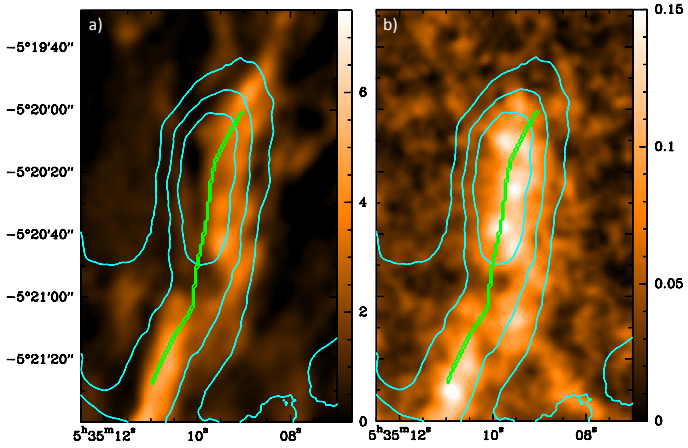

Fig. 9. Comparison of our ArTéMiS column density map (cyan contours) with (*a*) the ALMA+30m N_2H^+ moment-0 map from Hacar et al. (2018) and (*b*) the VLA+GBT NH_3 moment-0 map from Monsch et al. (2018) for the filament we associate with fibre 9. The ArTéMiS column density contours are 5, 7, and 9×10^{22} cm^{-2}. The green line shows the filament's crest as derived with DisPerSE.

larger-scale, velocity-coherent filaments in the inner Galaxy from the ATLASGAL 870 µm and SEDIGISM ^{13}CO(2–1) surveys (Schuller et al. 2009, 2017). These relatively shallow exponents indicate that the main filament features pronounced non-Gaussian wings of lower-density material that extend well beyond 0.1 pc from the ridge, as evident in Figs. 5–7. The profile of ISF-OMC-1 is strongly affected by the Orion-KL star-forming region, resulting in a somewhat steeper exponent.

The mean central H_2 densities inferred from our Plummer fits range from $\sim 4 \times 10^5$ cm^{-3} for OMC-3 and OMC-2 to $\sim 10^6$ cm^{-3} for OMC-1, assuming the ISF is in the plane of the sky (i.e. $i = 0$). The mean central density we infer for the OMC-1 portion of the ISF is a factor of three lower than the nominal volume density of 3×10^6 cm^{-3} found by Teng & Hirano (2020) for N_2H^+ filamentary structures in OMC-1 (outside of cores) through non-LTE modelling of the N_2H^+ (3–2) and (1–0) lines. Our dust continuum estimate of the volume density is, however, affected by a rather large uncertainty of a factor of ∼2–3 or more in the OMC-1 subregion, which is due to particularly uncertain dust opacity and temperature gradient effects in this unusually dense and strongly irradiated area (see e.g. Figs. A.1 and A.2). The N_2H^+ density estimates of Teng & Hirano (2020) are also uncertain by a factor of ∼3 (see their Table 3). Given these uncertainties, the two sets of density estimates are broadly consistent.

By integrating the radial profiles measured in the column density map of Fig. 3 over radii up to $D_{\rm HP}$ (i.e. twice the half-power radius), we also derived robust estimates of the mean mass per unit length of the inner portion of each ISF segment, excluding low-density material at large radii. The HGBS results suggest that most stars form within this inner portion of molecular filaments (e.g. Könyves et al. 2015, 2020). We obtain average values of ∼200 $M_\odot$ pc^{-1} for OMC-3, ∼250 $M_\odot$ pc^{-1} for OMC-2, ∼500 $M_\odot$ pc^{-1} for the OMC-1 portion, and ∼300 $M_\odot$ pc^{-1} for the whole northern ISF (i.e. OMC-1+OMC-2+OMC-3). For the filament shown in Fig. 9, which can be associated with fibre 9 of Hacar et al. (2018), we estimate a mean line mass of ∼100 $M_\odot$ pc^{-1} (see the column density profile in Fig. 10). These line mass estimates were validated via comparison with the low-resolution (5′) dust optical depth map of Planck Collaboration XI (2014). They are more than one order of magnitude higher than the line masses of the 'fertile fibres' observed in the nearby Taurus cloud (Hacar et al. 2013) and of the many transcritical filaments that dominate the filament line mass function (FLMF) in the Arzoumanian et al. (2019) HGBS sample (see Fig. 1 of André et al. 2019), but they are consistent with the bulk of confirmed Galactic filaments discussed by Mattern et al. (2018). Our measurements are also in agreement with the results of Schisano et al. (2020), who find a mean value of 250 $M_\odot$ pc^{-1} for a sample of 18 000 Galactic filaments with reliable distance estimates. It is not surprising to find such high line mass values in the Orion ISF since it is known to be undergoing fragmentation and ongoing embedded star formation (e.g. Takahashi et al. 2013; Teixeira et al. 2016).

4. Discussion

4.1. Density structure

The large-scale distribution of gas and dust in the northern part of Orion A is dominated by the ISF. Based on a column density map at 36″ resolution built from HGBS data, Stutz & Gould (2016) find that the radial distribution of gas near the ISF is well represented by a power law. They reported a line mass profile ($\lambda(w)$, in $M_\odot$ pc^{-1}) as a function of enclosing radius (w) in accordance with the following well:

$$\lambda(w) = K \left(\frac{w}{\rm pc} \right)^{\gamma}, \tag{8}$$

where $K = 385\ M_\odot$ pc^{-1} and $\gamma = 3/8$. This value of K was derived assuming the dust opacity law OH5 from Ossenkopf & Henning (1994), which roughly corresponds to the same dust opacity parameterisation as adopted in Sect. 3 but with $\beta = 1.8$ instead of $\beta = 2$. More precisely, the OH5 dust opacity at ArTéMiS wavelengths is a factor of ∼30% higher than the HGBS opacity law

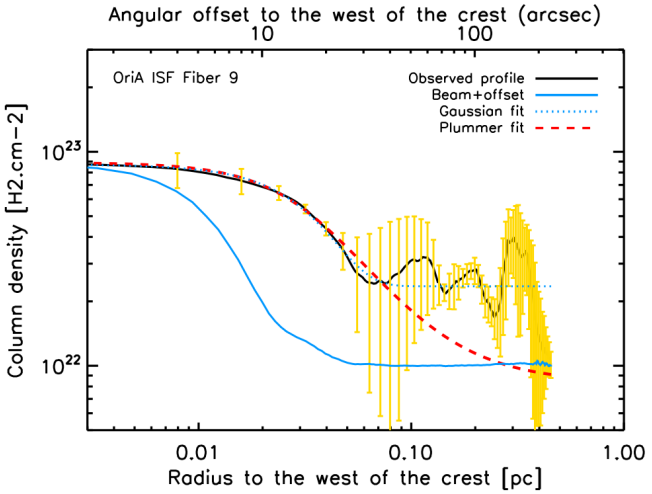

Fig. 10. Same as Fig. 5 but for the south-western side of the filament extracted with DisPerSE that coincides with fibre 9 of Hacar et al. (2018).

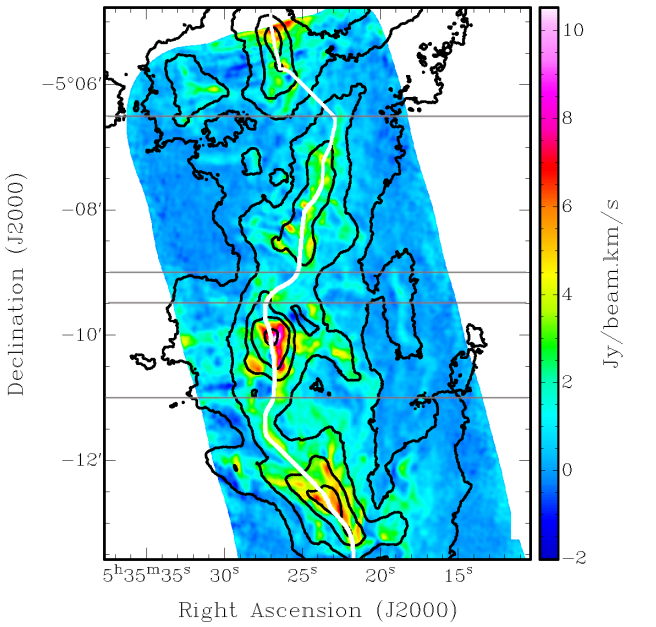

Fig. 11. ALMA N_2H^+ moment-0 map (from Hacar et al. 2018) overlaid with our H_2 column density map (black contours) for the ISF-OMC-2 region. The thick white line shows the crest of the filament extracted with DisPerSE. The thin horizontal lines indicate the limits of the various segments discussed in Sect. 4.2.1.

of Eq. (1). Equation (8) also corresponds to a line mass profile averaged over the full 1° length of the ISF, including a 0.4° long portion south of the field mapped with ArTéMiS, whose average column density is a factor of two or more lower than the northern part of the ISF discussed here, according to *Herschel* and *Planck* data. Considering these differences, the average line mass of ∼300 $M_\odot$ pc^{-1} that we derived in Sect. 3.4 for the northern part of the ISF, integrated over a transverse enclosing radius of $D_{\rm HP}$ ∼ 0.07–0.1 pc, is consistent with the value of K reported by Stutz & Gould (2016) for a radius of w = 1 pc.

The column density map used by Stutz & Gould (2016) is sensitive to scales between 0.05 and 8.5 pc. Based on our higher-resolution data, we find an inner plateau with a half-power width of order ∼0.06–0.11 pc (see Table 1). Therefore, while our results are consistent with the analysis of Stutz & Gould (2016), they allow us to resolve an inner break in the radial density and line mass profiles of the ISF that could not be seen with *Herschel* data only. From their analysis at 36″ resolution, Stutz & Gould (2016) did not find any significant variation of the column density profile along the extent of the ISF, but this is not surprising since they did not resolve the inner plateau in the density profile.

4.2. Comparison with high-density fibres

Although it is nearly impossible to associate each N_2H^+ fibre reported by Hacar et al. (2018) with the ArTéMiS/SPIRE filaments that we extracted with DisPerSE, we will now discuss a few examples.

4.2.1. ISF-OMC-2

First, we focus on the northern part of the ISF, where the main filament shows a relatively clear structure as compared to the highly complex network of filaments around the extreme region Orion-KL. The map published by Hacar et al. (2018) covers only $-05°25' \leq \delta \leq -05°05'$; therefore, we considered only the southern part of what we call ISF-OMC-2/3, which roughly corresponds to OMC-2. We analysed the radial column density profiles of different segments of the ISF, which correspond to different ranges in declination, as shown in Fig. 11. For each segment, we give the parameters of the best-fit Plummer and Gaussian models in Table 1, together with the range of FWHMs measured in N_2H^+ by Hacar et al. (2018) for each fibre that we tentatively associate with the ArTéMiS filaments (see also Fig. 4 for the numbering of the fibres).

The segment from $\delta = -05°11'$ to $\delta = -05°09'30''$, which roughly corresponds to fibre 43 from Hacar et al. (2018), contains the bright infrared source OMC-2 FIR 4. The values of the inner width that we measure for this segment ($D_{\rm HP}^{\rm Plummer}$ = 0.07 ± 0.025 pc) are in the lowest boundary of our sample. However, we caution the reader that this measurement is strongly affected by the presence of the centrally condensed protostellar source OMC-2 FIR 4 within this short segment (Shimajiri et al. 2008; López-Sepulcre et al. 2013). Assessing the intrinsic width of the underlying parent filament at this location is more uncertain. Nevertheless, such peculiar sources have very little effect on our estimates of the global properties of the ISF since we evaluated them from median radial profiles.

4.2.2. ISF-OMC-1

In the southern part of our ArTéMiS map, we also split the ISF into several segments, but only north of the HII region Orion-KL. We tentatively associated these segments with fibres seen in N_2H^+ (see numbering in Fig. 4). The inner widths as measured from Gaussian and Plummer model fitting are also given in Table 1, together with the FWHMs measured in the N_2H^+ data. Here also we derive inner widths significantly smaller than 0.1 pc for some portions of the main filament (e.g. the segment associated with fibre 21), where a dense protostellar core is embedded and locally affects our measurements.

4.2.3. Comparison between ArTéMiS and N_2H^+

We show in Fig. 12 the comparison between the $D_{\rm HP}^{\rm Plummer}$ diameters measured on our column density map and the FWHM of the N_2H^+ fibres that we associated with the different segments of the ISF, as listed in Table 1. This figure shows that there is

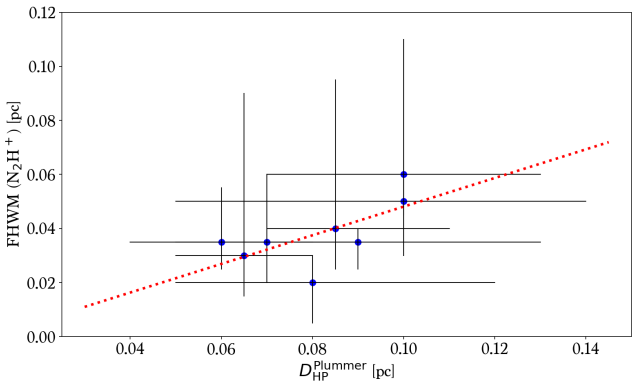

Fig. 12. Comparison between the inner widths ($D_{HP}^{Plummer}$) measured on the high-resolution column density map (Fig. 3) and the FWHM fitted on the associated fibres seen in N_2H^+. Each point is located at the average of the $D_{HP}^{Plummer}$ values measured eastwards and westwards of the crest vs. the median value of the fibre's distribution of FWHMs. The error bars indicate the full range of values on both axes. The dotted red line shows the position of a linear fit to the data.

a trend of increasing FWHM for the N_2H^+ fibres with increasing $D_{HP}^{Plummer}$: a linear fit to the data results in a slope of 0.53 (±0.24) and an intercept of −0.005 (±0.020); the Pearson correlation coefficient is equal to 0.66. Although the correlation is only marginal, we interpret this as an indication that N_2H^+ emission generally traces the densest portion along the central axis of the main filament.

Slight but significant deviations between the peaks in N_2H^+ emission and the filament crests traced by our sub-millimetre dust continuum data are visible in some cases, such as the filament associated with fibre 9 of Hacar et al. (2018, see our Fig. 9a). In that particular case, it is noteworthy that there is better agreement between the ArTéMiS-SPIRE filament and the filamentary structure detected in NH_3 by Monsch et al. (2018) at 6″ resolution (see Fig. 9b). At least in projection, fibre 9 lies between two large-scale H_2 'fingers' associated with the explosive CO outflow emanating from the immediate vicinity of Orion KL (cf. Zapata et al. 2009; Bally et al. 2017). The southern end of fibre 9 also overlaps with the area where high-velocity CO(6–5) emission was detected in the APEX observations of Peng et al. (2012). As CO is known to be a destroyer of N_2H^+ (e.g. Aikawa et al. 2001), it is possible that energetic finger-like outflow features may significantly reduce the abundance of N_2H^+ in the lateral edges of the dense filamentary structure. Strong anisotropic irradiation of fibre 9 by the Orion nebula (see e.g. the dust temperature map shown in Fig. 2) may also play a role via the desorption of CO molecules from grain mantles. In any event, a comparison of the N_2H^+ map of Hacar et al. (2018) with the NH_3 map of Monsch et al. (2018) clearly indicates that the abundance of N_2H^+ is far from uniform in the OMC-1 region. The most extreme difference between the two maps is that no N_2H^+ emission is detected in the immediate vicinity of Orion KL (see also Teng & Hirano 2020), presumably due to the destruction of N_2H^+ by CO, while strong NH_3 (1,1) and NH_3 (2,2) emission is seen in the Monsch et al. (2018) data and a prominent column density peak is observed in our data (cf. Figs. 1 and 3).

5. Conclusions

We have presented 350 and 450 µm observations with ArTéMiS of the ISF in Orion, the nearest site of active high- and intermediate-mass star formation. With angular resolutions of 8″ and 10″, the ArTéMiS data, combined with *Herschel*-SPIRE maps to recover large-scale emission, probe scales from 0.015 pc to a few pc. By combining the new ArTéMiS data with *Herschel* data at shorter wavelengths, we were able to build, for the first time, high-resolution temperature and column density maps covering a large region around OMC-1 that are not affected by saturation; these maps are publicly available from the CDS.

We extracted the radial profiles and intrinsic widths of several segments of the Orion ISF from the high-resolution column density map. Our conclusions can be summarised as follows.

- We resolve an inner plateau with a typical half-power width in the range 0.06–0.11 pc along the northern and southern parts of the main filament. This plateau could not be seen in the *Herschel*-SPIRE data alone because of their limited spatial resolution of ∼0.06 pc.
- These values of the inner width are consistent within better than a factor of two with the values measured in several nearby molecular clouds of the Gould Belt (Arzoumanian et al. 2011, 2019; Palmeirim et al. 2013) and in the massive star-forming complex NGC 6334 (André et al. 2016).
- The mean line masses that we derive from our data (between ∼100 and ∼500 $M_\odot\,pc^{-1}$) are in the extreme upper range of those found for *Herschel* filaments in the Gould Belt (Arzoumanian et al. 2019; André et al. 2019), as well as in the upper range of those measured for more than 18 000 filaments found in the Hi-GAL survey by Schisano et al. (2020). Our values are comparable to the line masses measured for larger-scale filaments throughout the Galaxy in the APEX/SEDIGISM survey (Mattern et al. 2018); this is consistent with the picture in which filament fragmentation and star formation occurs within the densest transcritical or supercritical portions of long, roughly ∼0.1 pc wide filaments.

The present study also highlights the importance of combining data that cover a wide range of spatial scales and of probing material at various densities. In particular, large high-resolution dust continuum maps with a high spatial dynamic range can efficiently trace a broad range of column densities, while complementary spectroscopic data are sensitive either to the densest inner regions of filaments (e.g. N_2H^+) or to the surrounding diffuse medium (e.g. CO and isotopologues).

Acknowledgements. We thank the anonymous referee for their detailed report, which helped us improving the robustness and the presentation of our results. We are very thankful for the continuous support provided by the APEX staff during ArTéMiS operations. F.S. acknowledges support from a CEA/Marie Sklodowska-Curie Enhanced Eurotalents fellowship. D.A. acknowledges support by FCT/MCTES through national funds (PIDDAC) by the grant UID/FIS/04434/2019. P.P. acknowledges support from FCT through the research grants UIDB/04434/2020 and UIDP/04434/2020. P.P. receives support from fellowship SFRH/BPD/110176/2015 funded by FCT (Portugal) and POPH/FSE (EC). Part of this work has received support from the European Research Council under the European Union's Seventh Framework Programme (ERC Advanced Grant Agreement no. 291294 – ORISTARS), from the French National Research Agency (Grant no. ANR–11–BS56–0010 – STARFICH), and from "Ile de France" regional funding (DIM-ACAV+ Program). We also acknowledge support from the French national programs of CNRS/INSU on stellar and ISM physics (PNPS and PCMI). The present study has made use of data from the *Herschel* Gould Belt survey (HGBS) project (http://gouldbelt-herschel.cea.fr). The HGBS is a *Herschel* Key Programme jointly carried out by SPIRE Specialist Astronomy Group 3 (SAG 3), scientists of several institutes in the PACS Consortium (CEA Saclay, INAF-IFSI Rome and INAF-Arcetri, KU Leuven, MPIA Heidelberg), and scientists of the *Herschel* Science Center (HSC). This document was prepared using the Overleaf web application, which can be found at www.overleaf.com.

References

Aikawa, Y., Ohashi, N., Inutsuka, S.-i., Herbst, E., & Takakuwa, S. 2001, ApJ, 552, 639
André, P., Bouwman, J., Belloche, A., & Hennebelle, P. 2003, in SFChem 2002: Chemistry as a Diagnostic of Star Formation, eds. C. L. Curry, & M. Fich (Ottawa, Canada: NRC Press) 127
André, P., Men'shchikov, A., Bontemps, S., et al. 2010, A&A, 518, L102
André, P., Di Francesco, J., Ward-Thompson, D., et al. 2014, Protostars and Planets VI (Tucson: University of Arizona Press), 27
André, P., Revéret, V., Könyves, V., et al. 2016, A&A, 592, A54
André, P., Arzoumanian, D., Könyves, V., Shimajiri, Y., & Palmeirim, P. 2019, A&A, 629, L4
Arzoumanian, D., André, P., Didelon, P., et al. 2011, A&A, 529, L6
Arzoumanian, D., André, P., Könyves, V., et al. 2019, A&A, 621, A42
Bally, J., Langer, W. D., Stark, A. A., & Wilson, R. W. 1987, ApJ, 312, L45
Bally, J., Ginsburg, A., Arce, H., et al. 2017, ApJ, 837, 60
Bernard, J.-P., Paradis, D., Marshall, D. J., et al. 2010, A&A, 518, L88
Bouwman, J., Meeus, G., de Koter, A., et al. 2001, A&A, 375, 950
Chibueze, J. O., Omodaka, T., Handa, T., et al. 2014, ApJ, 784, 114
Federrath, C. 2016, MNRAS, 457, 375
Güsten, R., Nyman, L. Å., Schilke, P., et al. 2006, A&A, 454, L13
Hacar, A., Tafalla, M., Kauffmann, J., & Kovács, A. 2013, A&A, 554, A55
Hacar, A., Tafalla, M., Forbrich, J., et al. 2018, A&A, 610, A77
Hildebrand, R. H. 1983, QJRAS, 24, 267
Johnstone, D., & Bally, J. 1999, ApJ, 510, L49
Koch, E. W., & Rosolowsky, E. W. 2015, MNRAS, 452, 3435
Kong, S., Arce, H. G., Feddersen, J. R., et al. 2018, ApJS, 236, 25
Könyves, V., André, P., Men'shchikov, A., et al. 2015, A&A, 584, A91
Könyves, V., André, P., Arzoumanian, D., et al. 2020, A&A, 635, A34
Lombardi, M., Bouy, H., Alves, J., & Lada, C. J. 2014, A&A, 566, A45
López-Sepulcre, A., Taquet, V., Sánchez-Monge, Á., et al. 2013, A&A, 556, A62
Malinen, J., Juvela, M., Rawlings, M. G., et al. 2012, A&A, 544, A50
Mattern, M., Kauffmann, J., Csengeri, T., et al. 2018, A&A, 619, A166
Men'shchikov, A. 2021, A&A, 649, A89
Menten, K. M., Reid, M. J., Forbrich, J., & Brunthaler, A. 2007, A&A, 474, 515
Molinari, S., Swinyard, B., Bally, J., et al. 2010, A&A, 518, L100
Monsch, K., Pineda, J. E., Liu, H. B., et al. 2018, ApJ, 861, 77
Nutter, D., & Ward-Thompson, D. 2007, MNRAS, 374, 1413
Ochsendorf, B. B., Brown, A. G. A., Bally, J., & Tielens, A. G. G. M. 2015, ApJ, 808, 111
Ossenkopf, V., & Henning, T. 1994, A&A, 291, 943
Palmeirim, P., André, P., Kirk, J., et al. 2013, A&A, 550, A38
Peng, T. C., Zapata, L. A., Wyrowski, F., Güsten, R., & Menten, K. M. 2012, A&A, 544, L19
Planck Collaboration XI. 2014, A&A, 571, A11
Polychroni, D., Schisano, E., Elia, D., et al. 2013, ApJ, 777, L33
Revéret, V., André, P., Le Pennec, J., et al. 2014, Proc. SPIE, 9153, 915305
Roussel, H. 2013, PASP, 125, 1126
Roussel, H. 2018, ArXiv e-prints [arXiv:1803.04264]
Roy, A., Martin, P. G., Polychroni, D., et al. 2013, ApJ, 763, 55
Roy, A., André, P., Palmeirim, P., et al. 2014, A&A, 562, A138
Sadavoy, S. I., Stutz, A. M., Schnee, S., et al. 2016, A&A, 588, A30
Salgado, F., Berné, O., Adams, J. D., et al. 2016, ApJ, 830, 118
Sault, R. J., Teuben, P. J., & Wright, M. C. H. 1995, ASP Conf. Ser., 77, 433
Schisano, E., Molinari, S., Elia, D., et al. 2020, MNRAS, 492, 5420
Schuller, F., Menten, K. M., Contreras, Y., et al. 2009, A&A, 504, 415
Schuller, F., Csengeri, T., Urquhart, J. S., et al. 2017, A&A, 601, A124
Shimajiri, Y., Takahashi, S., Takakuwa, S., Saito, M., & Kawabe, R. 2008, ApJ, 683, 255
Shimajiri, Y., Kawabe, R., Takakuwa, S., et al. 2011, PASJ, 63, 105
Shirley, Y. L. 2015, PASP, 127, 299
Smith, R. J., Glover, S. C. O., & Klessen, R. S. 2014, MNRAS, 445, 2900
Sousbie, T. 2011, MNRAS, 414, 350
Stutz, A. M., & Gould, A. 2016, A&A, 590, A2
Stutz, A. M., Tobin, J. J., Stanke, T., et al. 2013, ApJ, 767, 36
Stutz, A. M., Gonzalez-Lobos, V. I., & Gould, A. 2018, ArXiv e-prints [arXiv:1807.11496]
Suri, S., Sánchez-Monge, Á., Schilke, P., et al. 2019, A&A, 623, A142
Takahashi, S., Ho, P. T. P., Teixeira, P. S., Zapata, L. A., & Su, Y.-N. 2013, ApJ, 763, 57
Talvard, M., Revéret, V., Le-Pennec, Y., et al. 2018, SPIE Conf. Ser., 10708, 1070838
Teixeira, P. S., Takahashi, S., Zapata, L. A., & Ho, P. T. P. 2016, A&A, 587, A47
Teng, Y.-H., & Hirano, N. 2020, ApJ, 893, 63
Zapata, L. A., Schmid-Burgk, J., Ho, P. T. P., Rodríguez, L. F., & Menten, K. M. 2009, ApJ, 704, L45

Appendix A: Results derived with a modified dust opacity law

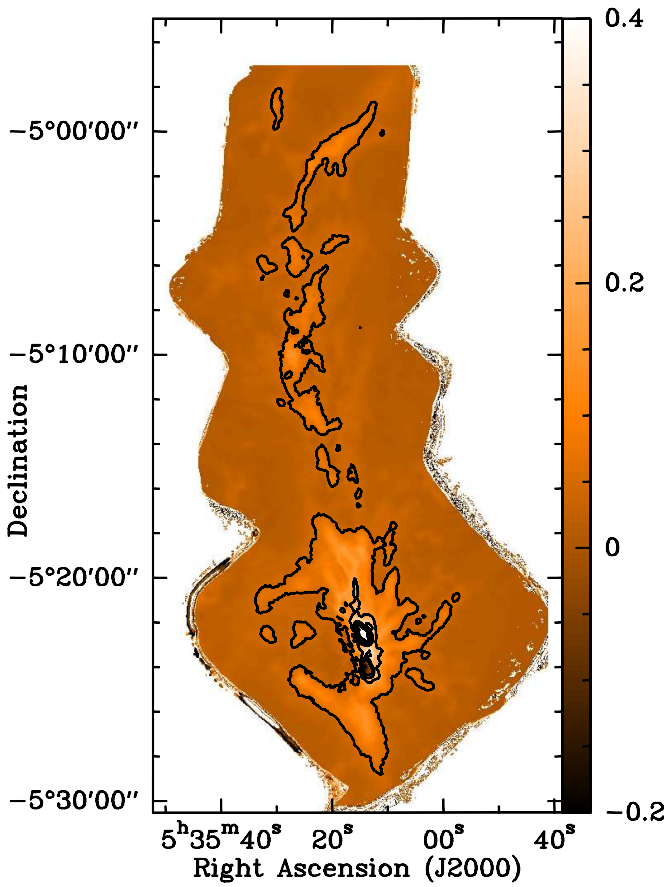

Fig. A.1. Map of the relative temperature difference, $(T_{\rm d}^{\rm alt} - T_{\rm d}^{\rm std})/T_{\rm d}^{\rm std}$, between the alternative dust temperature ($T_{\rm d}^{\rm alt}$), derived using the modified dust opacity law given by Eq. (3), and the standard dust temperature ($T_{\rm d}^{\rm std}$), derived using the HGBS opacity law of Eq. (1). Contours are +5%, +20%, and +35%.

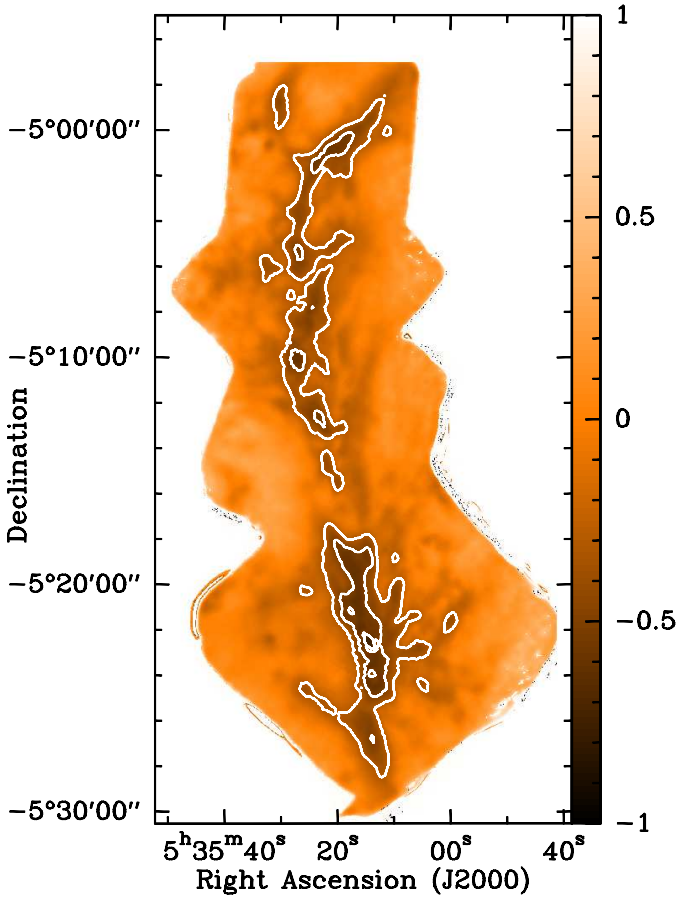

Fig. A.2. Map of the relative difference in column density, $(N_{\rm H_2}^{\rm alt} - N_{\rm H_2}^{\rm std})/N_{\rm H_2}^{\rm std}$, between the alternative column density ($N_{\rm H_2}^{\rm alt}$), derived using the modified dust opacity law given by Eq. (3), and the standard column density ($N_{\rm H_2}^{\rm std}$), derived using the HGBS opacity law of Eq. (1). Contours are −30%, −50%, and −70%.

In this section we present results derived from the alternative column density map, $N_{\rm H_2}^{\rm alt}$, computed using the modified dust opacity law given by Eq. (3) instead of a constant value for the dust opacity as expressed in Eq. (1). We show maps of the relative differences in the derived dust temperature and column density in Figs. A.1 and A.2, respectively. We measured the inner widths of the northern and southern parts of the main filament by fitting Gaussian and Plummer-like profiles to the $N_{\rm H_2}^{\rm alt}$ map, using the same method as described in Sect. 3.3.

The median radial intensity profiles computed for ISF-OMC-3, ISF-OMC-2, and ISF-OMC-1 are shown in Figs. A.3–A.5, respectively. The parameters of the best-fit models are reported in Table A.1, including the results obtained when splitting these filaments into small segments that can be associated with the fibres discussed by Hacar et al. (2018), as detailed in Sect. 4.2 and in Table 1.

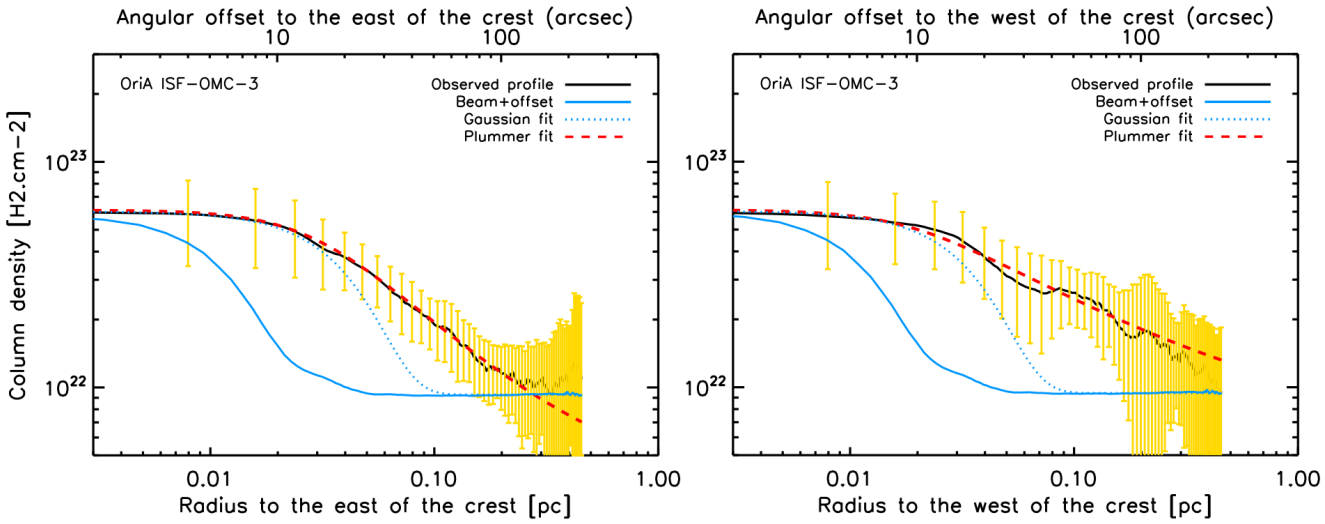

Fig. A.3. Median radial profiles for the northernmost part of the ISF (solid black curves) measured on the alternative column density map, on the eastern (*left panel*) and western (*right panel*) sides of the filament. The various lines have the same meanings as in Fig. 5.

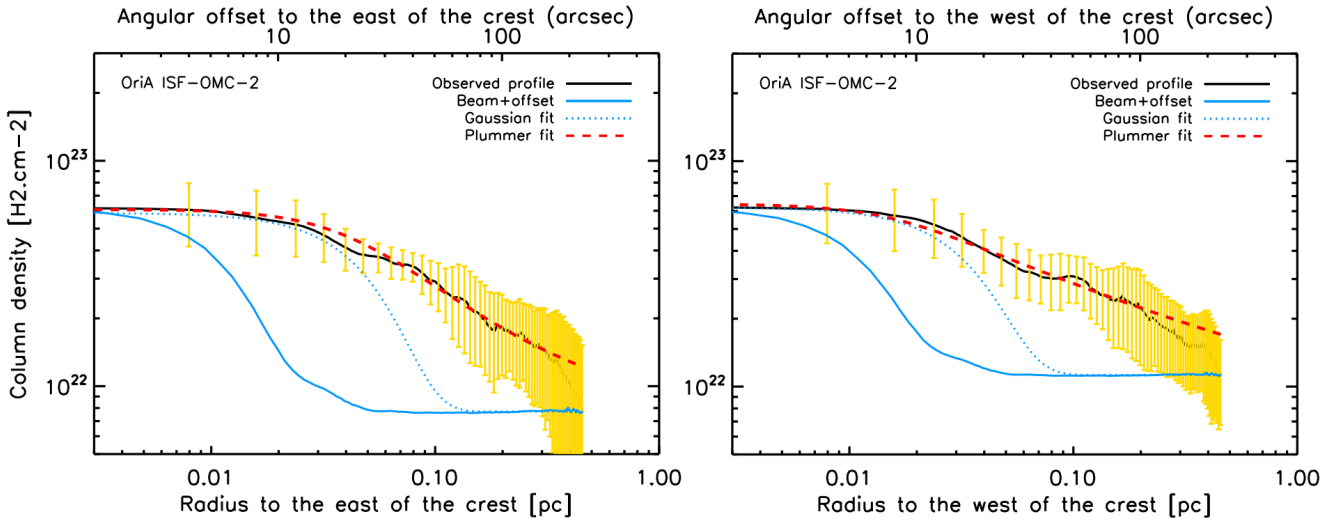

Fig. A.4. Same as Fig. A.3 but for the portion of the main filament covering OMC-2.

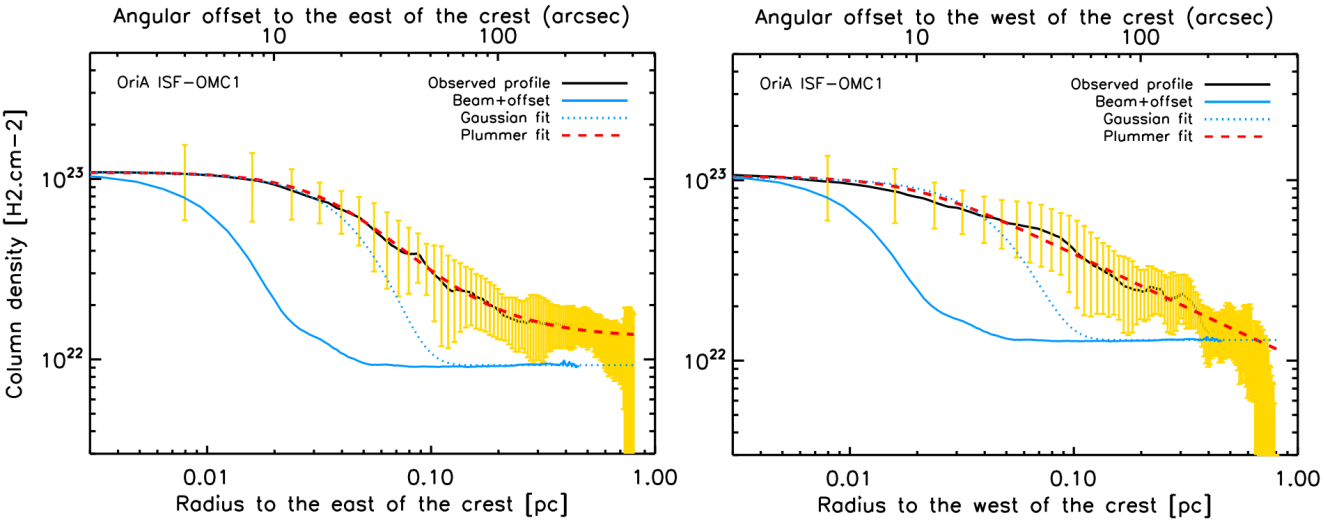

Fig. A.5. Same as Fig. A.3 but for the southern part of the main filament (ISF-OMC-1).

Table A.1. Median inner widths of selected filaments, as derived from both Plummer and Gaussian fitting to the radial profiles measured in the alternative column density map derived assuming the modified dust opacity law of Eq. (3).

Filament	$D_{\rm flat}$ (pc)	p	*FWHM* (pc)	$D_{\rm HP}^{\rm Plummer}$ (pc)
ISF-OMC-3				
West	0.045 ± 0.01	1.6 ± 0.3	0.06 ± 0.02	0.09 ± 0.01
East	0.06 ± 0.01	2.1 ± 0.2	0.07 ± 0.01	0.10 ± 0.02
ISF-OMC-2				
West	0.04 ± 0.02	1.5 ± 0.3	0.065 ± 0.02	0.10 ± 0.03
East	0.075 ± 0.02	2.0 ± 0.2	0.08 ± 0.02	0.13 ± 0.02
Fibre 41 (West)	0.05 ± 0.01	1.8 ± 0.2	0.05 ± 0.01	0.11 ± 0.02
Fibre 41 (East)	0.06 ± 0.02	1.7 ± 0.3	0.05 ± 0.02	0.10 ± 0.02
Fibre 44 (West)	–	–	–	–
Fibre 44 (East)	(0.07 ± 0.02)	(1.9 ± 0.3)	0.06 ± 0.03	0.12 ± 0.03
Fibre 43 (West)	(0.05 ± 0.02)	(1.8 ± 0.3)	0.06 ± 0.01	(0.09 ± 0.03)
Fibre 43 (East)	(0.05 ± 0.02)	(2.0 ± 0.3)	(0.09 ± 0.02)	(0.09 ± 0.02)
Fibre 37 (West)	(0.07 ± 0.03)	(2.0 ± 0.5)	(0.07 ± 0.02)	(0.12 ± 0.04)
Fibre 37 (East)	0.09 ± 0.03	2.3 ± 0.3	0.14 ± 0.03	0.15 ± 0.03
ISF-OMC-1				
West	0.04 ± 0.01	1.7 ± 0.3	0.08 ± 0.02	0.11 ± 0.02
East	0.05 ± 0.02	2.2 ± 0.3	0.08 ± 0.01	0.08 ± 0.02
Fibre 29 (West)	(0.05 ± 0.01)	(2.0 ± 0.5)	0.05 ± 0.01	(0.08 ± 0.02)
Fibre 29 (East)	(0.07 ± 0.02)	(2.1 ± 0.3)	0.07 ± 0.01	0.12 ± 0.02
Fibre 21 (West)	0.04 ± 0.02	1.8 ± 0.2	0.05 ± 0.01	0.10 ± 0.02
Fibre 21 (East)	(0.05 ± 0.02)	(2.0 ± 0.5)	0.06 ± 0.02	0.07 ± 0.01
Fibre 19 (West)	(0.09 ± 0.03)	(1.6 ± 0.4)	0.08 ± 0.02	0.16 ± 0.04
Fibre 19 (East)	(0.07 ± 0.02)	(2.0 ± 0.3)	0.06 ± 0.01	0.12 ± 0.03
Fibre 9 (West)	(0.04 ± 0.02)	(2.2 ± 0.5)	0.06 ± 0.01	0.07 ± 0.02

Notes. Values shown in parentheses denote cases with higher uncertainties in the fitted values.

Appendix B: Influence of the filament-finding algorithm

To check whether the choice of the algorithm employed to trace filament crests had any significant effect on our results, we used two alternative algorithms, *FilFinder* (Koch & Rosolowsky 2015) and *getsf* (Men'shchikov 2021), in addition to DisPerSE (Sousbie 2011) to define the spine of the ISF. Figure B.1 shows the results. Although *getsf* tends to break up filamentary structures into smaller pieces than the other two algorithms, it can be seen that the three methods agree quite well in all three portions (OMC-1, 2, and 3) of the ISF.

Moreover, the three distributions of individual widths measured along the whole ISF using the three sets of crests are very similar (see Fig. B.2). A Kolmogorov-Smirnov test confirms that the distribution of widths found with the DisPerSE crests (Fig. 8) is statistically indistinguishable from the other two distributions.

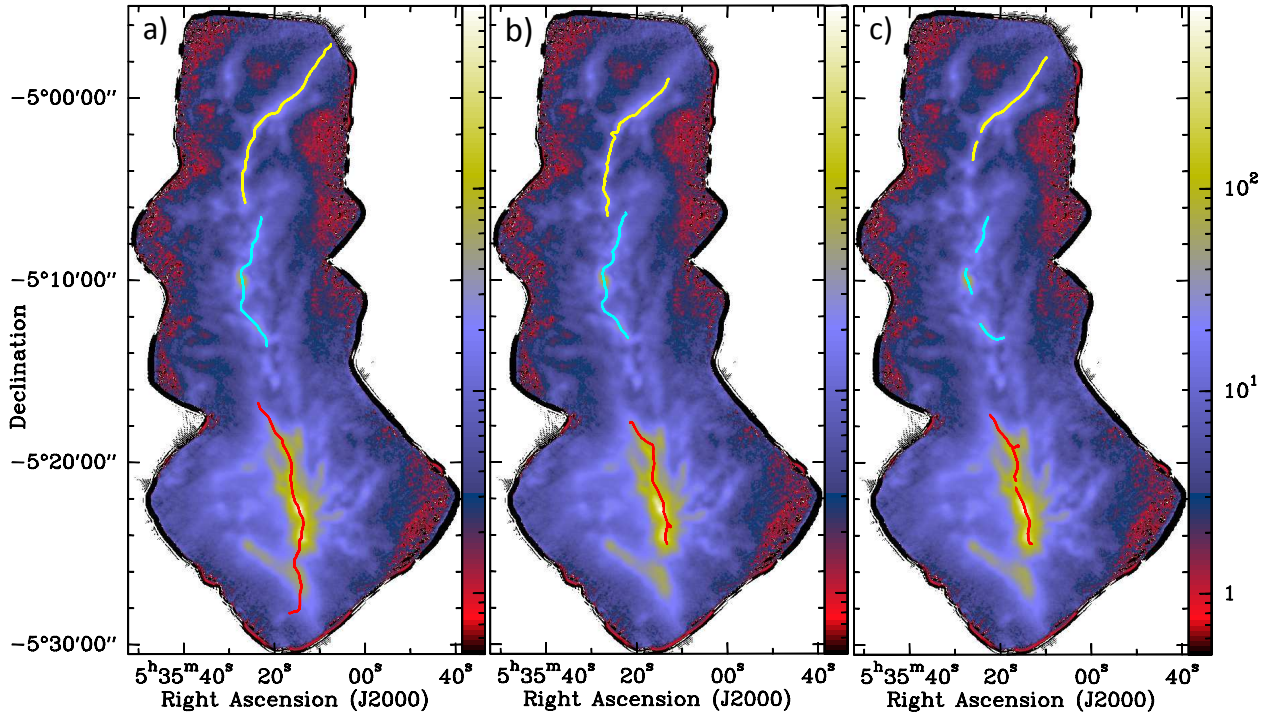

Fig. B.1. Comparison of the crests derived for the ISF (from top to bottom: OMC-3 portion in yellow, OMC-2 in cyan, and OMC-1 in red) using three different filament-finding algorithms: DisPerSE (*a*), *FilFinder* (*b*), and *getsf* (*c*). The underlying image is the same ArTéMiS + SPIRE 350 μm map as shown in Fig. 4.

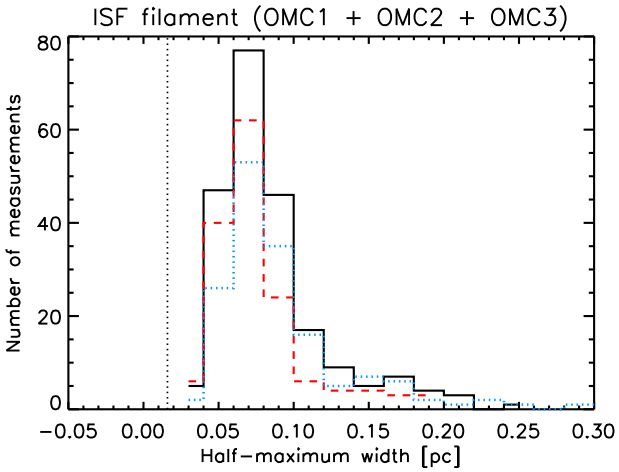

Fig. B.2. Comparison of the distributions of individual width measurements along the whole (OMC-1 + OMC-2 + OMC-3) ISF obtained using the crests defined by DisPerSE (same solid black histogram as in Fig. 8), *FilFinder* (dotted blue histogram), and *getsf* (dashed red histogram).

Appendix C: Influence of temperature variations along the line of sight

To evaluate the effect of temperature gradients along the line of sight on our results, we constructed synthetic images for a model filament with a Plummer-type density distribution (Eq. (4) with $p = 2$) and a realistic temperature distribution, assuming an ambient interstellar radiation field (ISRF) typical of the Orion region ($G_0 = 1000$)[1]. The cylindrical model filament was assumed to have a central column density of $N_0 = 2 \times 10^{23}$ cm^{-2} on its crest, an intrinsic half-power diameter of $D_{\rm HP} = 0.075$ pc, and an outer diameter of 0.55 pc. It was also assumed to be embedded in a background cloud of column density $N_{\rm bg} = 9 \times 10^{21}$ cm^{-2} and, for simplicity, to lie in the plane of sky. The properties of this model filament are roughly similar to those derived for the ISF (see Sect. 3 and Table 1). The synthetic dust temperature profile within the model filament was calculated for $G_0 = 1000$ using an analytic approximation formula on a grid of radiative transfer models performed with the MODUST code (see Bouwman et al. 2001 and André et al. 2003). Two sets of synthetic emission maps for the model filament were generated at all observed *Herschel* and ArTéMiS wavelengths, assuming optically thin dust emission with the nominal dust opacity law given by Eq. (1) on one hand ('C.1 test') and the alternative dust opacity law given by Eq. (3) on the other hand ('C.2 test'). Column density and dust temperature maps were then produced from these synthetic emission maps in the same manner as for the real data, by fitting a modified blackbody to the observed SEDs on a pixel-by-pixel basis and assuming the same nominal dust opacity law in both cases (cf. Sect. 3.1). The purpose of the C.2 test is to assess the combined effect of line-of-sight temperature gradients and dust opacity uncertainties.

The results of this experiment and a comparison with the input model are provided in Figs. C.1 and C.2, in the form of radial temperature and column density profiles, and in Table C.1. As expected, it can be seen in Figs. C.1a and C.2b that the temperature profiles derived from SED fitting (green curve) overestimate the intrinsic dust temperature profile of the model (black curve). This is due to the fact that the model filament is colder in its inner interior and that the temperatures derived from

[1] The radiation field in the OMC-1 subregion is somewhat higher than the value adopted in the model described here. Accordingly, the internal dust temperature gradient within the OMC-1 portion of the ISF and the corresponding effects on the OMC-1 column density profiles may be somewhat stronger than shown in Figs. C.1 and C.2.

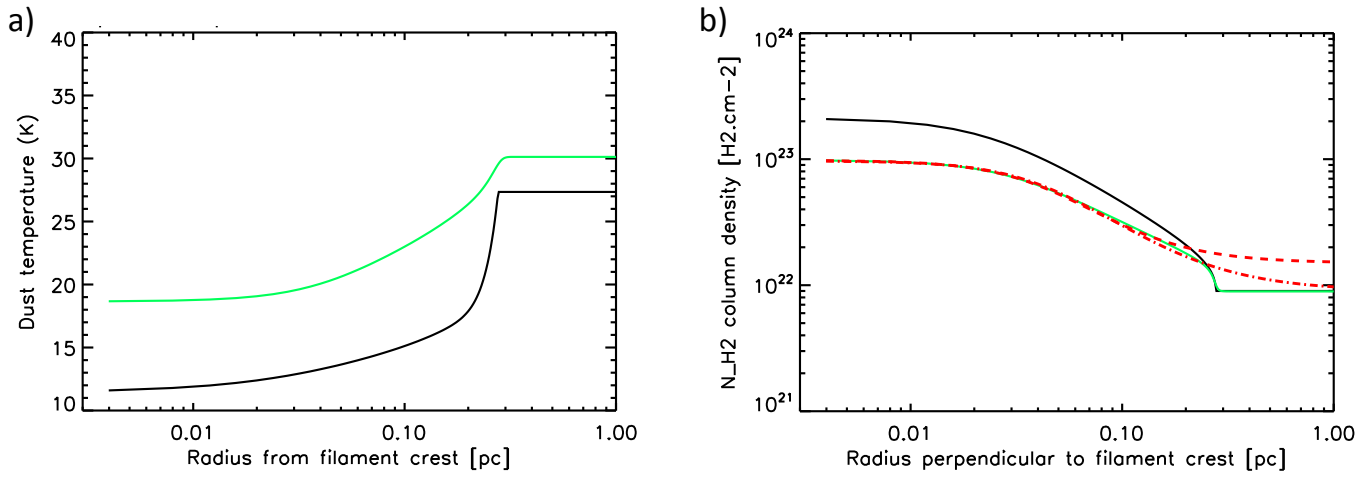

Fig. C.1. Synthetic dust temperature (*a*) and column density (*b*) profiles of a model filament with Plummer-type density structure, illustrating the effect of temperature gradients along the line of sight. The true dust opacity law and the dust opacity law adopted to derive temperature and column density maps from synthetic emission maps were identical and given by Eq. (1). *(a)* Comparison between the intrinsic model temperature profile as a function of radius (black curve) and the temperature profile as a function of projected radius resulting from SED fitting and thus averaging along the line of sight (green curve). *(b)* Comparison between the corresponding model column density profile (black curve) and the column density profile resulting from SED fitting (green curve). The dashed and dash-dotted red curves represent two Plummer fits to the SED column density profile, which differ only from each other and from the model in the outer regions.

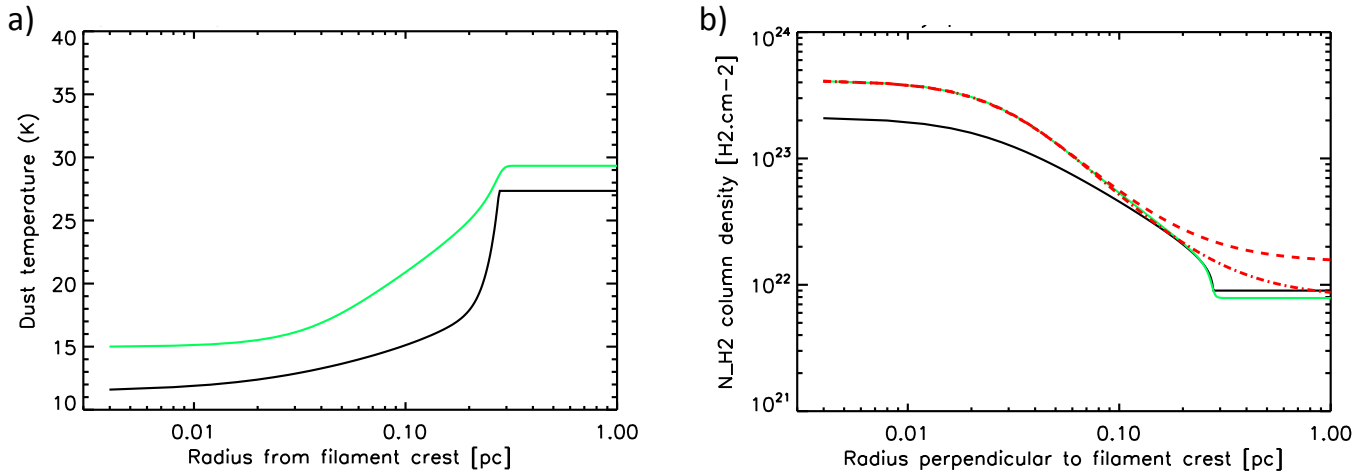

Fig. C.2. Same as Fig. C.1, for the same model filament but assuming the true dust opacity law is given by Eq. (3) while the dust opacity law adopted to derive temperature and column density maps from SED fitting is given by Eq. (1).

Table C.1. Results of measurement tests using synthetic maps of a Plummer model filament.

Filament	N_0 (cm^{-2})	$D_{\rm flat}$ (pc)	p	$D_{\rm HP}$ (pc)
Model	2.1×10^{23}	0.046	2	0.075
C.1 fit	0.9×10^{23}	0.080–0.082	2.7–2.5	0.09–0.10
C.2 fit	4.2×10^{23}	0.027–0.028	2.75–2.74	0.06–0.062

SED fitting represent line-of-sight averages that are significantly affected by the warmer outer layers of the filament. Accordingly, the column density profile derived assuming the correct dust opacity (green curve in Fig. C.1b) underestimates the intrinsic column density profile of the model (black curve in Fig. C.1b) by a factor of 2.3 at small radii. In the C.2 case, on the other hand, the temperature effect does not quite compensate for the incorrect assumption about the dust opacity, and the derived column density profile (green curve in Fig. C.2b) still exceeds the intrinsic column density profile (black curve in Fig. C.2b) by a factor of two at the centre of the filament.

The shape of the derived column density profiles is nevertheless very similar to the shape of the model column density profile. Consequently, the half-power diameters derived from Plummer fits to the SED-based column density profiles (red curves in Figs. C.1b and C.2b) remain close to (within 30% of) the true half-power diameter of the input model (see Table C.1). More precisely, the derived $D_{\rm HP}$ diameter overestimates the intrinsic half-power diameter of the model (0.075 pc) by only ∼30% in test C.1 and underestimates it by only ∼20% in test C.2. By comparison, the derived central column density and p index values are more uncertain and affected by larger systematic errors (see Table C.1). These tests demonstrate that line-of-sight averaging effects have only limited impact on the filament width measurements reported in Sect. 3.